

Remote Sensing of Submerged Oceanic Turbulence and Fossil Turbulence

Carl H. Gibson

*Departments of Mechanical and Aerospace Engineering
and Scripps Institution of Oceanography,
University of California San Diego, La Jolla CA 92093-0411, USA
E-mail: cgibson@ucsd.edu, <http://www-ac.scs.ucsd.edu/~ir118/>*

Valery G. Bondur

*Aerocosmos Scientific Center of Aerospace Monitoring, Moscow, Russia
E-mail: vgbondur@online.ru*

R. Norris Keeler

*Directed Technologies, Inc., Arlington, VA 22201, USA
E-mail: norris_keeler@directedtechnologies.com*

Pak Tao Leung

*Department of Oceanography, Physical Section
Texas A&M University, College Station, TX 77843, USA
E-mail: ptleung@tamu.edu, <http://mae.ucsd.edu/~ptleung/>*

Abstract

Microstructure and internal-wave measurements from vertical and horizontal profilers near a Honolulu municipal wastewater outfall are compared to soliton-induced sea-surface brightness anomalies from optical and synthetic-aperture-radar space satellite images. Spectral anomalies with wavelengths 30-1000 m were detected September 2, 2002. Anomaly areas covered 70 km² in 10 km and 5 km SW and SE lobes extending from the diffuser. Studies in 2003 and 2004 increase the range of detection to 20 km from the outfall in areas covering 200 km². The remote detection mechanism indicated by these remarkable observations is a complex interaction between advected 10 m outfall fossil turbulence patches and internal-soliton-waves (ISWs). ISWs supply new turbulent-kinetic-energy to outfall patches near the pycnocline depth. Energy, mixing, and information is radiated near-vertically by both the primary and secondary fossil turbulence patches in ISW patterns of surface smoothing, as detected from space. Nonlinear vertical-amplification

and vertical-beaming internal wave processes are similar to those of astrophysical masers but more efficient. Off shore advection of the outfall fossil turbulence patches required to produce the anomaly lobes varies widely and unpredictably, and depends on fresh water run off from the island.

Keywords: Turbulence, diffusion, and mixing processes, Fine structure and microstructure, Nearshore processes, Remote sensing.

Introduction

Three international oceanographic experiments RASP (Remote Anthropogenic Sensing Program) have been carried out in August-September, 2002, 2003, and 2004 involving several ships, space satellites, helicopters, and a variety of environmental sensors, Keeler, Bondur, Gibson (2005), hereafter KBG. The objective of the experiments has been to evaluate and monitor space satellite methods to remotely detect submerged turbulence and fossil turbulence from the Sand Island wastewater outfall in Mamala Bay, Honolulu, Hawaii. Synoptic mean and microstructure measurements were carried out to explore possible physical mechanisms. In this paper we emphasize optical imagery of sea surface glint brightness from sun synchronous satellites Ikonos and Quickbird, but include comparisons with synthetic aperture radar (SAR) images. Energy and intermittency constraints beyond the scope of the present paper are discussed in Gibson, Bondur, Keeler and Leung (2006, GBKL).

Approximately $3\text{-}4\text{ m}^3\text{ s}^{-1}$ of relatively low density ρ_w , low salinity S , treated wastewater is pumped 2.4 km offshore from Sand Island through a 1.98 m pipe and discharged by 283 horizontal jets from both sides and the end of a 1,040 m long diffuser section at bottom depths 68 to 71 meters. Buoyant oily surfactants are completely removed by the treatment process. No evidence was found of ambient surfactants on the sea surface or any effects on the present results by surfactants (except for a localized oil spill from the ship anchorage September 14, 2003, discussed in GBKL). Trapping of the wastewater depends on its strong initial dilution with dense bottom water by the diffuser jets. If the bottom water volume B to wastewater volume W initial dilution ratio $B/W \geq (\rho_s - \rho_w)/(\rho_B - \rho_s)$, the jets rise and merge to form a buoyant turbulent plume with density intermediate between the densities of the surface ρ_s and bottom ρ_B receiving waters. The wastewater plume typically rises to a trapping depth about 50 m below the sea surface, just below the seasonal pycnocline depth.

Figure 1a (top) shows outlines of spectral brightness anomaly areas detected during the RASP experiments, Bondur (2005b). The shapes of the anomaly areas and their close proximity to the diffuser section of the effluent pipe indicate that the anomalies are caused by the Sand Island outfall. The 10 km and 5 km SW and SE anomaly regions from September 2, 2002, cover 70 km^2 in advection directions determined by parachute drogues. The single lobe area in Fig. 1a (top) from September 13, 2003 extends more than 20 km to the SW and covers 200 km^2 , and the corresponding SAR outfall anomaly extends to 40 km and covers more than 800 km^2 ,

Fig. 4 (bottom). Anomaly areas in Fig. 1a (top) from 2004 are truncated to the west by limits of the satellite images.

A submerged turbulence detection mechanism termed beamed-zombie-turbulence-maser-action (BZTMA) is discussed in KBG and GBKL. Physical processes, hydrodynamic-phase-diagrams, and microstructure evidence of multiple secondary turbulence events from a fossil turbulence patch are given in Gibson (1987). The BZTMA mechanism is enhanced if fossil turbulence patches locally become larger or more numerous than in ambient areas. Fig. 1a (bottom) shows an ERS-1 SAR image of tidally generated internal solitary waves (ISWs) produced at the New York Bight continental shelf and enhanced over the Hudson Canyon, Apel (2002).

Transmission of ISW images to the sea surface, and enhancement over topography, is explained by the BZTMA mechanism. BZTMA is powered by turbulence patches that radiate most of their turbulent kinetic energy at fossilization vertically as large amplitude breaking internal waves because the damped turbulence motions are close to overturning at the ambient stratification frequency N . Images of the ISWs and images of fronts crossing over Hudson Canyon, Fig. 1a (bottom), are enhanced in intensity by waves from secondary-turbulence formed on the more numerous fossil turbulence patches generated by such bottom-topography turbulence-generated vertical nonlinear internal waves. Breaking fossil turbulence waves and breaking secondary fossil turbulence waves smooth the sea surface above Hudson Canyon and reveal its presence, and enhance surface manifestations of any other source of submerged stratified turbulence such as the ISWs and the fronts.

Figure 1b (top), Bondur (2005b), shows an anomaly map a) for Quickbird, September 3, 2004, compared to internal wave measurements from thermistor strings inside the anomaly area d) and near shore e). Four resolved narrow-band 43-160 m internal waves measured by thermistor string T5 south of the diffuser can be identified with four of the five surface brightness anomaly wavelengths in b). The 43-160 m quasimonochromatic surface brightness anomalies are not found in background area c) and appear much attenuated in the near shore thermistor measurements of e). Fig. 1b (bottom) shows a schematic of the complex experiments, measurement section paths, and the satellites, ships, and sensors employed in RASP 2004, Bondur (2005b).

How is it possible for such multiple, small-scale, narrow-band, randomly-oriented soliton-like, internal waves to exist on the thermocline? How does their signature appear in the sea surface brightness anomaly regions associated with the Sand Island outfall, as shown in Figs. 1a (top) and 1b (top)? The waves appear to be a previously unknown form of internal-solitary-wave (ISW), independent of tides and with much smaller scales than tidal coastal lee wave ISW packets discussed in the literature, Apel (2002), Bogucki, et al. (2005), Boguki et al. (1997), Maxworthy (1979), Moum et al. (2003), Moum and Smyth (2005), where such 200-500 m (and larger) wavelength ISWs are bore-like features that ride on shallow pycnoclines and have surface manifestations (slicks, Suloy) easily detectable by SAR or by eye. How is it possible for deep ocean features such as seamounts and ISWs they generate to be detected by SAR and by astronauts? A large collection of ISW and bottom topography images and a review of ISW theory by Apel (2002) is available at <http://www.internalwaveatlas.com>.

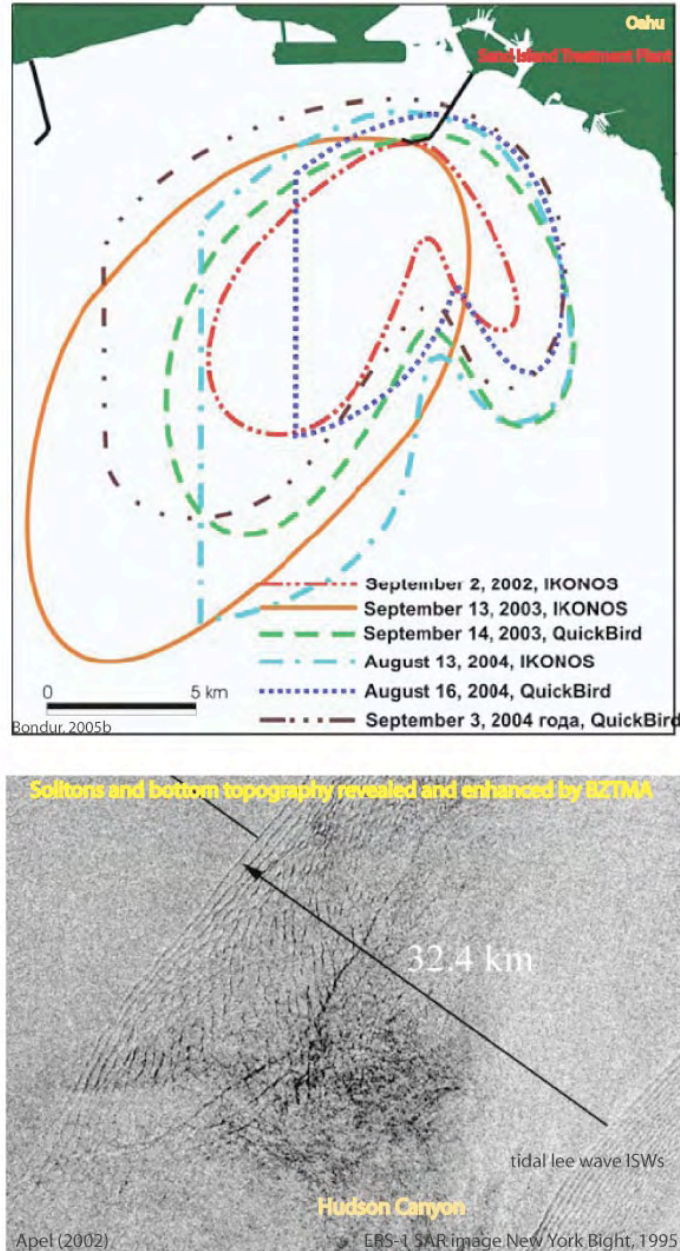


Figure 1a: (top) Spectral quasimonochromatic anomaly regions (λ wavelengths 30-250 m) detected from optical satellite images during the remote anthropogenic sensing program RASP 2002, 2003, 2004, Bondur (2005b). The anomaly regions reflect enhancement by the BZTMA mechanism, KBG. (bottom) Radar image showing that surface manifestations of ISWs and several fronts are enhanced over Hudson Canyon by turbulence patches from FTWs radiated vertically from bottom turbulence.

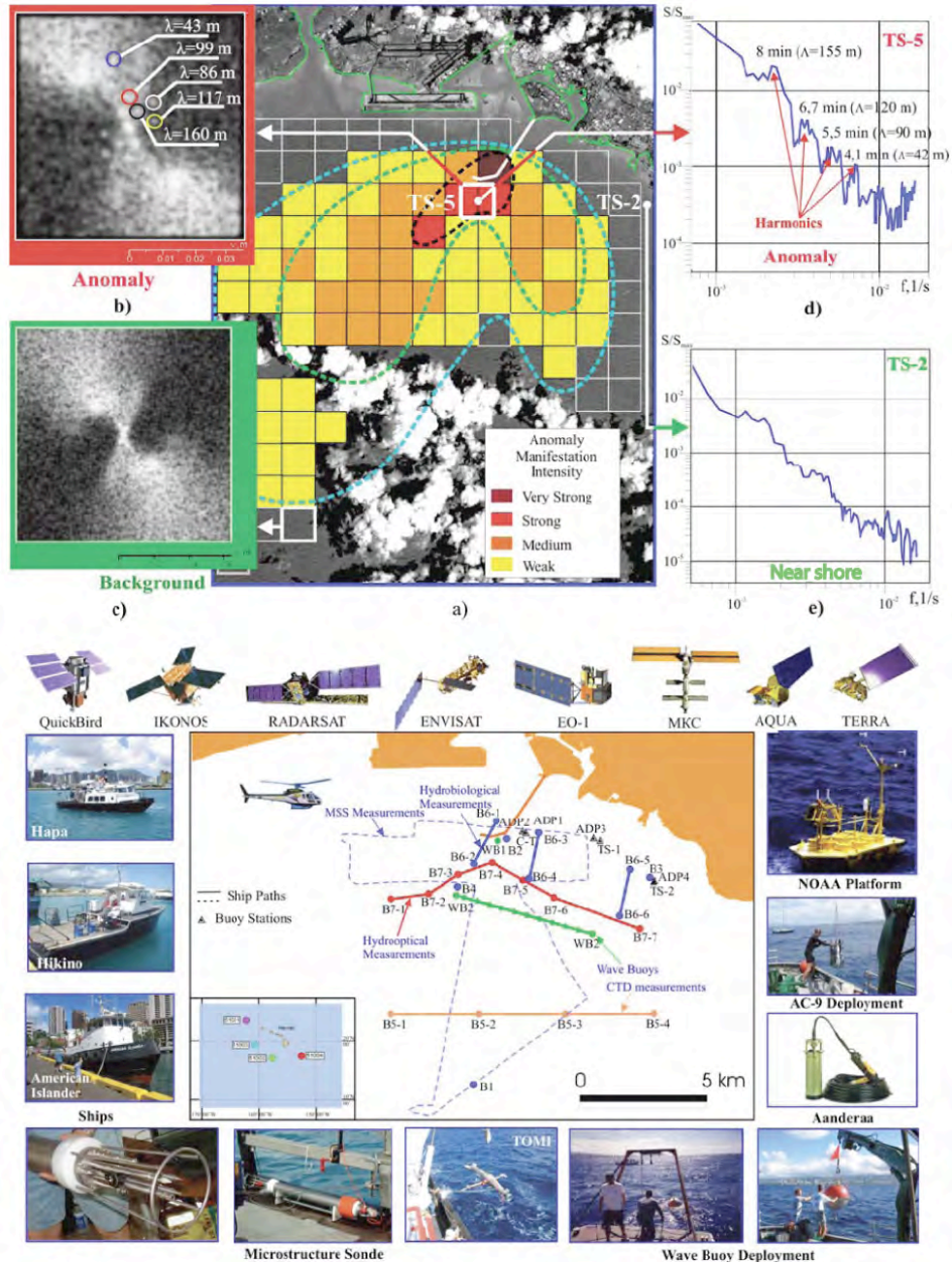


Figure 1b: Sea surface brightness anomaly map for Sept. 4, 2004, QuickBird image and internal wave spectra from thermistor strings TS-5 and TS-2. Wavelengths λ of the anomalies match wavelengths Λ of the internal waves at TS-5's position just south of the diffuser and at TS-2 nearer shore (top). The complex array of ships, satellites, microstructure detectors, platforms, and section paths used in RASP 2004 is shown (bottom), Bondur (2005b).

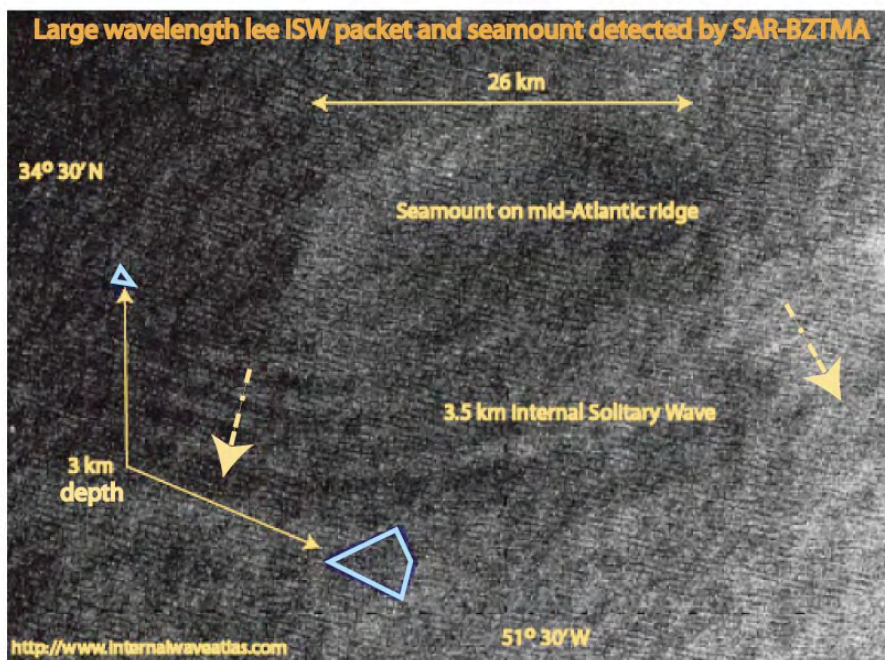
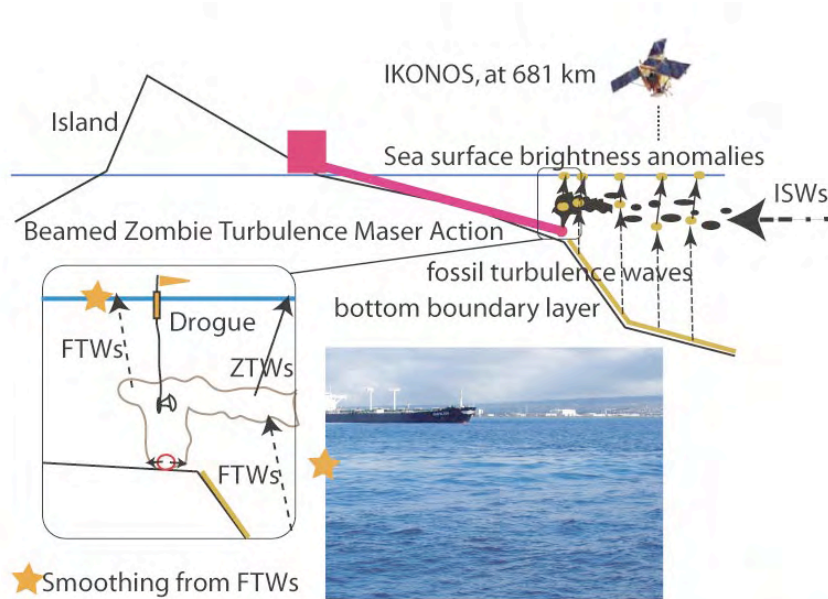


Figure 1c: Schematic of RASP experiments and the BZTMA detection mechanism. A photograph (top) from the ship (HAPA) positioned over the west end of the diffuser pipe shows evidence of surface smoothing ~50 m to the NW by fossil turbulence waves with no evidence of continuous vertical turbulent mixing (no discoloration, smell, or continuous microstructure in vertical profiles). Lee wave ISW solitons with $\lambda > \text{depth}$ are an alternative source of narrow-band forcing at the pycnocline. BZTMA (bottom) is needed to explain how SAR and optical images of lee wave ISW packets and mid-Atlantic seamounts can be detected by radar and astronauts.

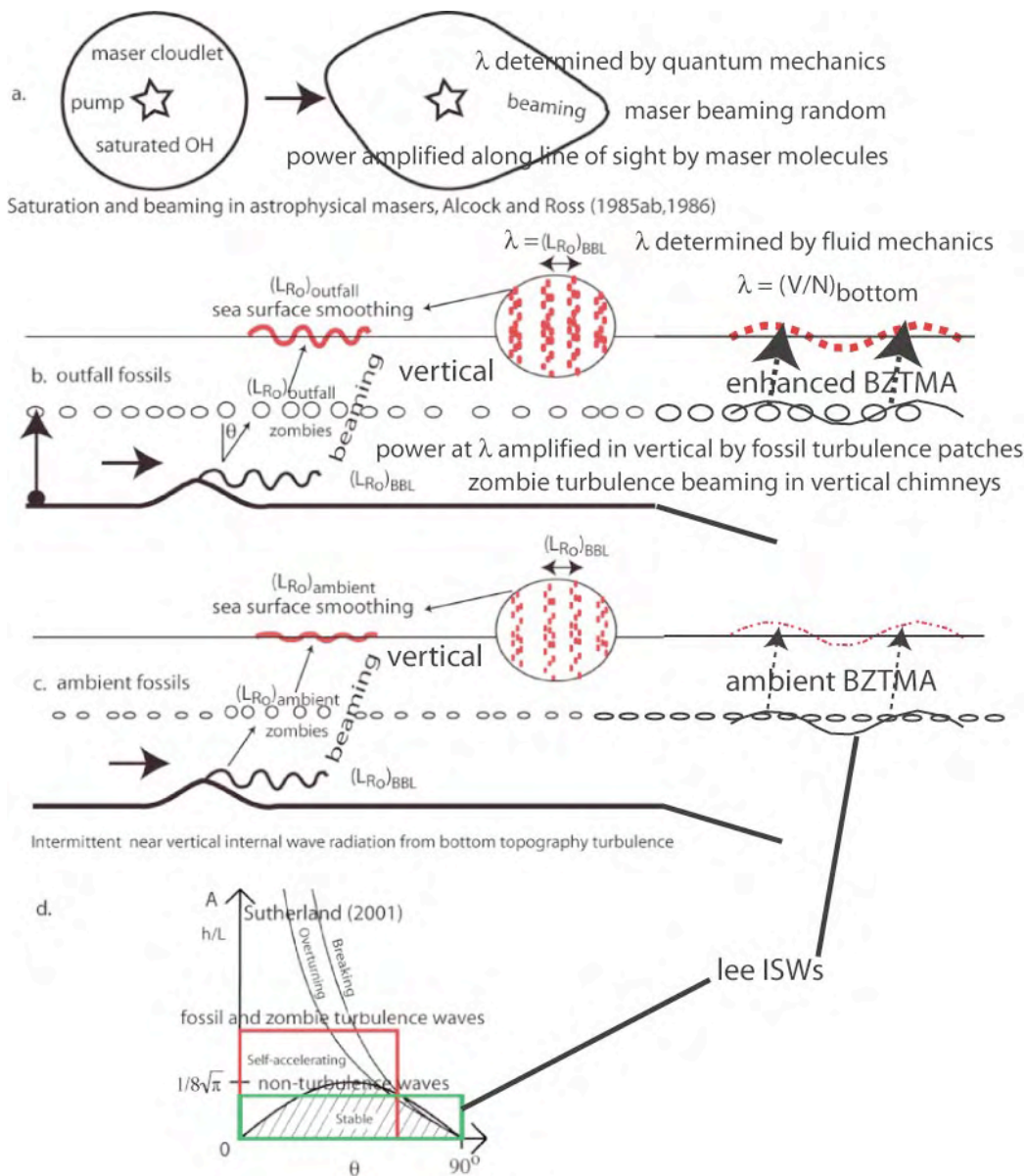


Figure 1d: Beamed-zombie-turbulence-maser-action (BZTMA) model for remote detection of submerged turbulence, modified from KBG to include large- λ tidal lee ISWs. Quantum mechanics determines the frequency of the electromagnetic waves amplified along lines of sight in astrophysical masers. Fluid mechanics determines the frequency of ISWs, beamed vertically in BZTMA. Non-linear beaming in astrophysical masers occurs in random directions. Non-linear beaming in BZTMA occurs vertically in mixing chimneys, GBKL.

Many answers to these questions not considered in the ISW literature are provided by theoretical, numerical and laboratory studies of turbulence in contact with stably stratified fluids, Linden (1975), Sutherland and Linden (1998), Sutherland (2001), Dohan and Sutherland (2003), Sutherland, Flynn and Dohan (2004), Flynn and Sutherland (2004). These studies show near vertical angle ($\sim 45^\circ$) radiation of narrow spatial-frequency-band internal waves, termed Linden-Sutherland waves (LSWs) in KBG, from stratified turbulence regions. Large amplitude versions of LSWs penetrate far above their sources to produce herringbone clouds, sinusoidally bumpy airplane rides, and narrow frequency band OH sky brightness patterns in the stratosphere.

From the fossil turbulence theory of Gibson (1980) and the theory and deep ocean evidence of Gibson (1986, 1987) it follows that such waves are caused by fossil-vorticity-turbulence internal-wave-motions (FVTWs) as they decay at the largest overturning scale permitted by the ambient stable-stratification N ; that is, the Ozmidov scale at beginning of stratification $L_{R_o} = (\epsilon_o / N^3)^{1/2}$, Gibson (1980). The viscous dissipation rate ϵ_o at beginning of fossilization occurs when inertial vortex forces $\vec{v} \times \vec{\omega}$ of the growing, overturning, turbulence eddies are matched by ambient buoyancy forces and converted to fully saturated, fossil-vorticity-turbulence internal waves.

FVTWs cannot radiate because their frequency is N . As friction slows them down they can couple to the stratified ambient fluid above and below a fossil turbulence patch. This produces large-amplitude, near-vertically radiated fossil turbulence waves as the bobbing frequency decreases. Most of the turbulent kinetic energy of a stratified turbulence patch at high Reynolds number will be radiated near-vertically, and most of the turbulent kinetic energy of secondary turbulence events absorbed from ambient tilting motions will be radiated near-vertically when the secondary turbulence fossilizes.

Pinkel et al. (2002) note that acoustic scattering strength is strongly increased above deep water tidal solitons, and that the effect persists for some hours. They refer to the fossil salinity turbulence remnants that cause the enhanced scattering as an acoustic dye. The enhanced vertical mixing and strong surface wave damping reported by Pinkel et al. (2002) over the passing solitons give clear evidence of the BZTMA mechanism for remote sensing of submerged turbulence.

The studies of Linden, Sutherland and colleagues are closely related to an analysis of oceanic microstructure by Gibson (1987) who proposed that the Caldwell (1983) paradox “Ocean turbulence: big bangs or continuous creation?” can best be resolved by a merged, sequential, vertical, cascade process termed “... big bangs and continuous creation”. This process is indicated by microstructure measurements in the deep ocean, Gregg (1977ab). In the Gibson (1987) scenario, fossil density turbulence patches extract energy from ambient internal waves to produce secondary and higher order turbulence events with approximately the same Cox number. Therefore the same normalized Reynolds number at fossilization $Re_o / Re_F = \epsilon_o / \epsilon_F = \epsilon_o / 30\nu N^2$ is achieved by the secondary events, reversing the -1/3 direction of decay of a fossilizing patch on a hydrodynamic phase diagram to a +1/3 trajectory for secondary turbulence, as shown in KBG (see Fig. 11).

Using this interpretation, a 32 m thick microstructure region (TASADAY 11 MSR 20) at 878-910 m depths from Gregg (1977ab) is interpreted as one primary turbulence event and five or more secondary turbulence events (see Fig. 8 [bottom]). Each secondary turbulence event fossilizes and re-radiates large-amplitude near-vertical LSWs. Leung and Gibson (2004) and KBG have called these zombie-turbulence-waves (ZTWs) to indicate their secondary nature. This apt terminology was invented by Professor Hide Yamazaki to describe velocities produced in computer simulations of initially frozen fossil density turbulence after gravity is turned on.

From Apel (2002), tidal lee waves of depression can set the scale of ISWs, Maxworthy (1979). So can stratified turbulence, as shown by Farmer and Armi (1999) in Knight Inlet, where turbulence at the Ozmidov scale at fossilization produce narrow-band FTWs at scale L_{R_o} and these are trapped on the pycnocline.

Vertical radiation of information about submerged turbulence by a sequence of vertically-oriented, secondary-turbulence-events, with re-radiation in the vertical by ZTWs that preserve wavelength information about their energy source, is closely analogous to the nonlinear physical processes of beamed masers in astrophysics.

In a beamed maser (or in a laser pointer), a molecule like OH^- (water missing its proton) is pumped to a metastable quantum energy state by an energy source; for example, powerful radiation heating by a nearby star in an astrophysical maser. Photons with the frequency of the metastable quantum state trigger a cascade of re-radiation at the particular frequency (wavelength) in the line of sight to the star, amplified in strength by many orders of magnitude (up to 10^6) above the star black body radiation level. Because this secondary radiation can also pump molecules from ground state to the metastable state, the source energy may cascade to give maser beams.

Similarly, decayed fossil density turbulence patches can absorb ISW energy and beam and amplify it vertically in quasimonochromatic patterns that preserve the ISW wavelength for remote detection. The process was termed beamed-zombie-turbulence-maser-action (BZTMA) in Leung and Gibson (2004), with detailed discussion from RASP measurements in KBG and GBKL.

Figure 1c (top) schematically illustrates the process as it has emerged as a working hypothesis in the RASP program. Surface smoothing observed with enhanced mixing over the outfall diffuser without continuous vertical turbulence clearly proves that FTWs produced by submerged stratified turbulence smooth the sea surface. GPS drogue paths prove that outfall fossil turbulence patches are advected into the brightness anomaly regions illustrated in Fig. 1a (top) and Fig. 1b (top) to provide enhanced amplification of ZTWs.

Fig. 1c (bottom) shows SAR images of a seamount at 3 km depths on the mid-Atlantic ridge south of the Azores with 3.5 km wavelength lee internal solitary waves at less than 3 km depths that have not and cannot be explained by the usual speculations about surfactants and induced linear convergences. The first astronauts claiming they could see such topographical features in the deep ocean were not believed. However, such images are easily understood using the BZTMA vertical information transport mechanism.

Figure 1d shows a comparison of the BZTMA model of vertical internal wave beaming to the non-linear amplification of narrow-frequency-band radiation along lines of sight by astrophysical masers. In masers the wavelength amplified along lines of sight is determined by quantum mechanics. For ISWs the wavelength amplified in the vertical direction is determined by fluid mechanics.

ISWs are produced either by FTWs at L_{R_0} scales or by lee waves at V/N scales. Figure 1d is KBG (2005 Fig. 3) modified to include lee wave ISWs. Lee ISWs are large-wavelength small-amplitude waves described by the “non-turbulent” wave portion of the Sutherland (2001) stability diagram (bottom left).

Even small amplitude lee ISWs with $h/L < 1/8\sqrt{\pi}$ must have sufficiently large Reynolds number to generate FTWs at scales smaller than V/N to produce surface manifestations. FTWs and ZTWs initially have $h/L \sim 1$, or 14 times larger than the maximum stable value $1/8\sqrt{\pi}$.

The internal wave maser actions of oceanic BZTMA are much more efficient than those of quantum mechanical masers. Most of the turbulent kinetic energy for the high Reynolds number events driving BZTMA is beamed vertically. Only a small fraction of the energy required to pump molecules to metastable states in astrophysical masers is converted to narrow-band maser frequency radiation.

Further discussion of field, laboratory, and numerical simulations of mechanisms for remote detections of submerged turbulence is given in the final discussion section of this paper, following presentation of the RASP 2002 observations. Details of microstructure and satellite observations from RASP 2003 and 2004, further discussion of available energy sources, and evidence of intermittent ZTW beaming in vertical mixing chimneys are beyond the scope of the present paper and are provided by GBKL.

Satellite Images and Brightness Anomaly Patterns

Figure 2 shows the IKONOS-2 Mamala Bay image from which the September 2, 2002, spectral anomaly detection of submerged turbulence and fossil turbulence was computed. Two-dimensional Fourier transforms of the sea surface brightness are shown for 2 km squares representing Background and Outfall influenced sea surface brightness. Anomalously bright spectral points shown in Fig. 2 Outfall image b correspond to Fourier elements (double dots represented by a double arrow) with wavelengths of 105 m oriented EW that are present but much weaker in Background image a.

The NW surface swell is not aligned with this spectral component even though it has a similar wavelength. This 105 m wavelength is larger than any fossil outfall turbulence patch detected, and larger than the depth of the outfall. These observations imply that an EW ISW with $\lambda \approx 105\text{m}$ exists on the pycnocline, such as those reported in Fig. 1b (d), Bondur (2005b). These ISWs are likely pycnocline trapped waves from vertical (FTW) internal wave packets from a bottom boundary layer turbulence source to the east or west, as shown in Fig. 1c (top) and Fig. 1d (b left) but could be small lee wave solitons as shown in Fig. 1c (bottom) or Fig. 1d (b right).

Grey stripes from the SW with 1000 m separation shown by arrows are similar to the 500 m tidal lee ISWs of Moum et al. (2003), and are interpreted as outfall enhanced lee wave ISWs in Fig. 2. The grey stripes are more pronounced in the region of the SW lobes of Fig. 1a and Fig. 3, consistent with information of their presence being moved to the sea surface by outfall fossils near the pycnocline depth by the outfall-enhanced BZTMA mechanism. Information about tidal forcing, microstructure, hydrography, and ambient conditions at larger scales near Oahu in Sept., 2002, are given by Alford et al. (2006).

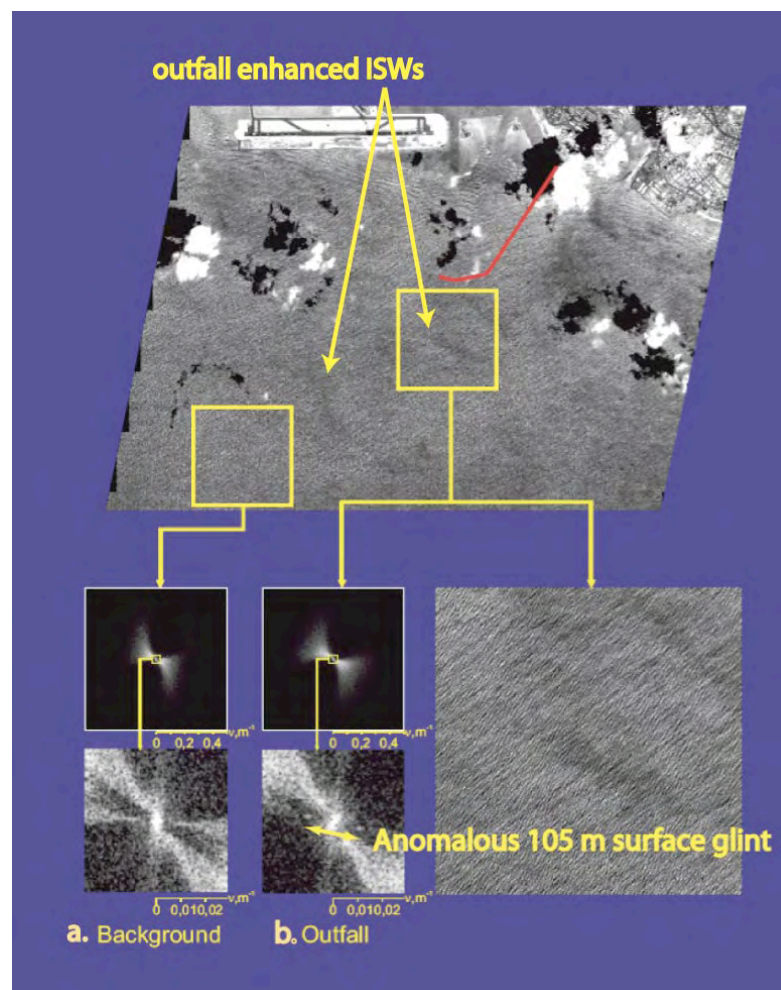


Figure 2: Optical image of Mamala Bay sea surface glint from Ikonos-2 satellite at noon Sept. 2, 2002. Analysis from 2 km square patches a. Background and b. Outfall shows anomalously bright Fourier elements just south of the diffuser oriented EW with 105 m wavelengths (double arrow). Grey areas just south of the diffuser indicate large wavelength tidal lee ISWs with surface manifestations enhanced by outfall fossils and the BZTMA mechanism.

Figure 3 gives a fragment map of sea surface brightness anomalies computed by using phase spectrum and random texture synthesis methods, Bondur and Filatov (2003). These methods involve the formation of model images from ambient data and two-dimensional Wiener spatial spectra of the brightness field and randomly generated phase spectra, Bondur and Savin (1995). By complex remote sensing computational procedures the 1 km square anomaly fragments of Fig. 3 were formed and color coded in four levels of anomaly intensity from Weak to Very-Strong. Strong and Very-Strong anomalies were found up to 3 km south of the diffuser, with Very-Strong fragments 13 and 14 at 3 km.

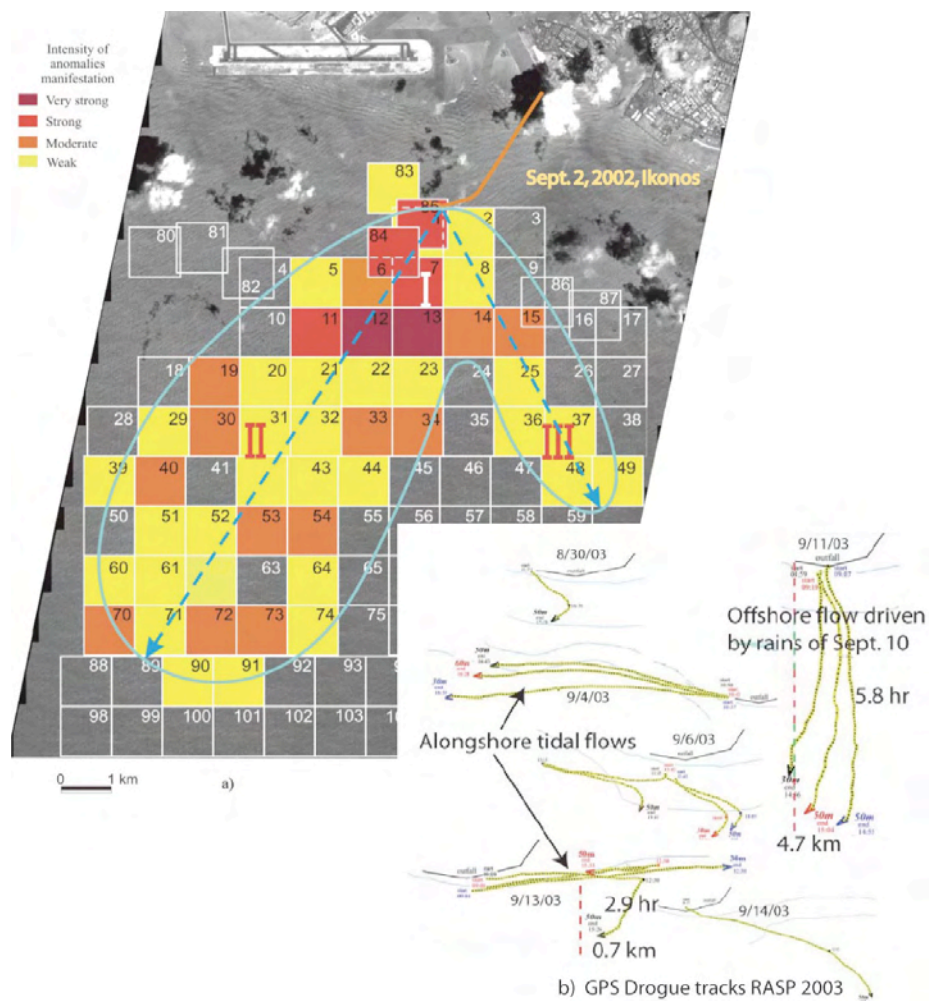


Figure 3: Spatial distribution (a) of anomalous spectral brightness caused by submerged outfall turbulence in 1 km areas from the 9/2/2002 Ikonos space image of Fig. 2, Bondur and Filatov (2003). Drogues set at the outfall trapping depth drifted into region 2 to the SE, opposite to the NW ship drift (see Fig. 16). The SW and SE anomaly lobes reflect the advection of outfall fossil turbulence patches as shown in (b) by a collection of GPS equipped parachute drogue tracks, where the weighted parachutes of the drifters were inserted at 30 and 50 m, near the trapping depth.

Microstructure advected in this direction is likely to be 5-15 hours old with origin below the trapping depth, from the available drogue track information (see Fig. 16) and from ADCP progressive vector diagrams. Moderate intensity fragments 70, 72 and 73 to the SW were at ~ 10 km, indicating a microstructure age of over a day or at least 260 N^{-1} . Strong and weak fragments 83 and 85 and the lack of any anomaly fragments on the east end of the diffuser reflect the northwest drift of surface layers that advect embedded fossil turbulence waves before they reach the surface.

The glove shaped form of Fig. 3 has been reproduced frequently, as shown in Fig. 1a, and can be attributed to fresh water induced off-shore drift of the outfall fossil turbulence patches, as shown by the GPS equipped parachute drogue tracks collected in RASP 2003 at bottom right of Fig. 3 (see also Fig. 6). Continuous fresh water streams to the ocean from Oahu are to the NW of the outfall (Pearl Harbor) and NE (Ala Wai canal).

Figure 4 shows spectral anomaly regions for the largest anomaly region detected in all of the RASP experiments so far, from 9/13/2003, extending 20 km to the SW and covering an area of $\sim 200 \text{ km}^2$. The green oval in fragment 14 marks the location of a BZTMA mixing chimney (discussed in GBKL), and the dashed white line marks the location of a mixing front detected by vertical and horizontal microstructure profiling (also discussed in GBKL, but shown in formation by the SAR image at the bottom of Fig. 4 from 9/11/2003), detected from vertical and horizontal profiles 7 km south of the outfall and discussed in GBKL. Many large anomaly wavelengths (100-220 m) are observed at 10 km compared to only one (Fig. 2) or two (30-100 m) wavelengths (Fig. 5) found at < 3 km. The flood of outfall fossils from the rainwater induced offshore advection produced the 40 km RADARSAT anomaly shown at the bottom of Fig. 4 the day after the rains, and the 20 km spectral anomaly pattern of Fig. 4 (top) two days later. Powerful outfall triggered BZTMA vertical information transfer and mixing on 9/11/2003 reveal bottom topography features to the SE of Diamond Head, and several strong mixing fronts in Mamala Bay south of the outfall and Waikiki. The random orientations of the spectral anomaly elements, double arrows and dots Fig. 4 (top), shows that they are not surface manifestations of ISWs radiated by, and therefore pointing toward, the outfall source.

Figure 5 shows a smaller region of spectral anomalies, detected 9/2/2003. The smaller size anomaly region (compared to other anomaly regions in Fig. 6) is attributed to the lack of comparably large off shore flow rates. Surface fragments with the strongest spectral anomalies were close to the outfall and indicated relatively small ISW wavelengths of only 32 and 53 meters. Similar results from RASP 2004 were observed, showing small off shore flows, small spectral anomaly regions, and small anomaly wavelengths (30-160 m), to be reported elsewhere.

Figure 6 (top) shows areas of spectral anomalies compared to drogue tracks and tidal cycles a few days previous to the large anomaly region, Fig. 4 (top), and the small anomaly region, Fig. 5. The large anomaly (yellow dashed line) extends 20 km to the SW of the outfall, and is attributed to strong anti-estuarine off-shore advection of outfall fossil turbulence patches induced by rainfall and BZTMA vertical mixing, as indicated by the drogue tracks of 9/11/2003 (bottom panel). Weaker off-shore flows (middle panel) preceded the small anomaly region of 9/2/2003 (dashed black line).

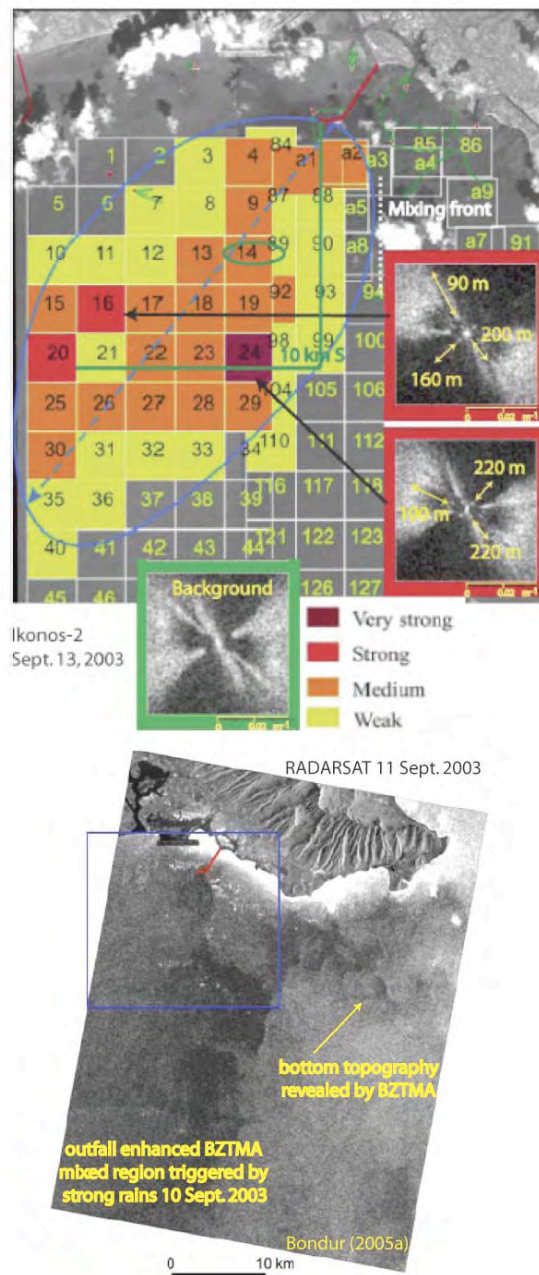


Figure 4: (top) Spectral anomaly regions detected 9/13/2003. The surface brightness spectral anomaly region extends 20 km to the SW of the outfall, and is attributed to strong offshore advection induced by rains on 9/10/2003. (bottom) The RADARSAT SAR outfall mixing anomaly of 9/11/2003 extends over 40 km to the south, leaving the mixing front (dashed line top) detected 9/13/2003 by vertical and horizontal microstructure sections, GBKL. Bottom topography features to the SE of Diamond Head are revealed by the outfall enhanced vertical transport of information to the sea surface.

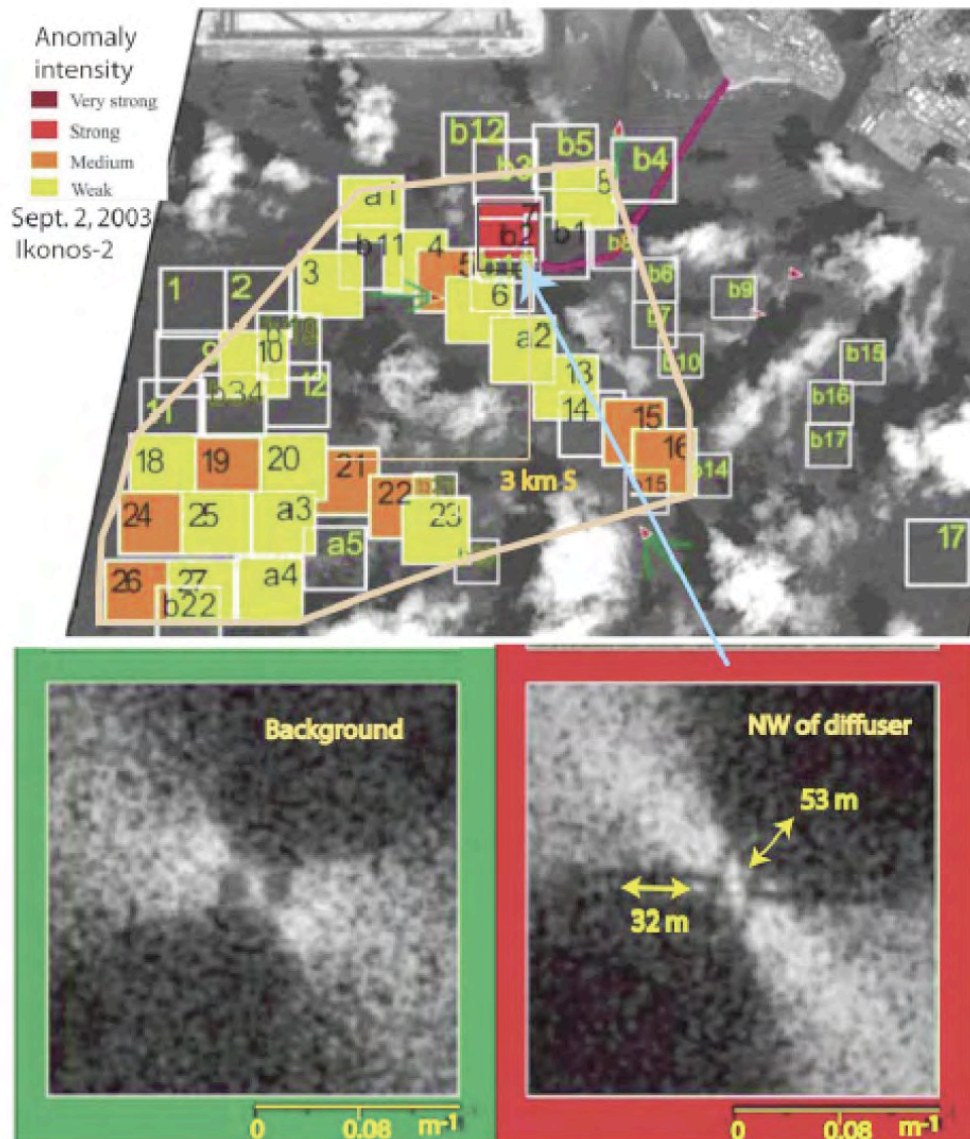


Figure 5: Spectral anomaly regions detected 9/2/2003. The anomaly region extends only 8.6 km to the SW of the outfall. The small extent is consistent with indications of relatively weak offshore advection (see the following Fig. 6 middle panel). The small wavelengths (32 m and 53 m) suggest these ISWs are likely produced by bottom FTWs at Ozmidov scales rather than lee wave depression ISWs at V/N scales.

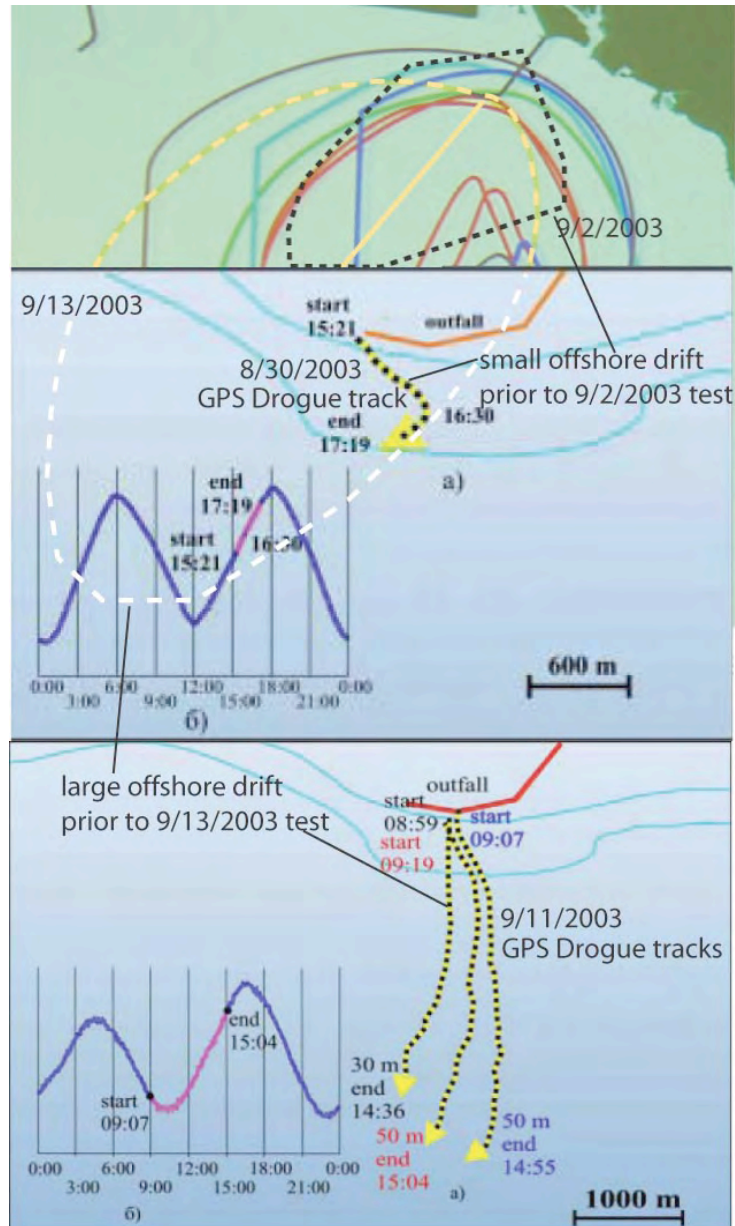


Figure 6: Areas of spectral anomalies (top panel) reported by V. Bondur at UCSD workshop Mar. 9-11, 2005 (Bondur 2005a), compared to drogue tracks and tidal cycles a few days previous for the largest anomaly region 9/13/2003 and for the smallest anomaly region 9/2/2003. The large single lobe anomaly (yellow dashed line top, Fig. 4) extends 20 km to the SW of the outfall, and is attributed to off-shore advection of outfall fossil turbulence patches induced by rainfall 9/10/2003, as indicated by the GPS drogue tracks of 9/11/2003 at bottom. Weaker off-shore flows (middle panel) preceded the small anomaly region of 9/2/2003 (dashed black line top panel, Fig. 5).

Vertical Microstructure Profiles

Figure 7a shows vertical profiling stations and times near the outfall pipe after the 9/2/2002 Ikonos-2 satellite overflight at noon. Two modified Sea & Sun Technology MSS instruments (MicroStructure Measurement System, MSS) were used to horizontally and vertically profile the mean conductivity, temperature and depth as well as the microstructure parameters temperature-gradient, velocity-shear, micro-conductivity, turbidity and fluorescence, Wolk et al. (2004), Fig. 1b (bottom left). The basic MSS instrument and the method of vertical deployment is described by Prandke and Stips (1998). A similar profiler and the turbidity and fluorescence sensor used in the modified MSS is discussed by Wolk et al. (2002). The MSS sonde is dropped over the side of the drifting ship and the neutrally buoyant sensor cable is paid out and carefully kept slack by an operator controlled winch as the weighted sensor package descends at a constant velocity of 0.7 m s^{-1} . Signals are recorded and monitored in the ship laboratory. GPS navigation permits precise positioning of profiling stations along the diffuser pipe and nearby.

Our study represents the first microstructure description of the hydrodynamic behavior and performance of an oceanic municipal outfall. The continuous source of strong, stratified, oceanic turbulence provided by the outfall gives a rare opportunity to make sufficient repetitive oceanic sampling to achieve statistical convergence of stratified turbulence parameters as they evolve, and the possibility for repeated future tests for reproducibility. The Thorpe overturning scale L_T profiles show clear evidence of fossil turbulence wave (FTW) mixing patches above both the outfall turbulence and the wastewater trapping depth (dashed line). Increased mixing rates above the trapping depth near the outfall (confirmed by the towed MSS measurements at 37 m depth, Fig. 16) compared to ambient rates are attributed to outfall enhanced BZTMA vertical radiation and mixing. This interpretation is supported by anomaly patch 83 of Fig. 3 (a) NW of the diffuser pipe end. Evidence of FTW and ZTW near-surface breaking is shown by vertical microstructure profiles at the outfall and from horizontal profiling above the buoyancy trapped wastewater, where larger overturning scales and larger dissipation rates are found near the surface and over the trapped wastewater plume than in ambient profiles.

Figure 7b compares the near surface viscous dissipation rates for profiles G4060001 and G4060002 near the end of the diffuser in the direction of the ship drift, to ambient profiles G4070001 and G4070002 west of the diffuser and G4030001 and G4030002 to the east. An increase above ambient viscous dissipation rate levels by two orders of magnitude is indicated for the upper 10 meters of the water column. Because there is no continuous vertical turbulent mixing, horizontal shears, wind variation or alternative explanation, the observed effect is attributed to outfall fossil turbulence wave and zombie turbulence wave breaking at the 10 m deep wind mixing pycnocline.

Observations from the ship and photographs such as that in Fig. 1c prove that near-vertical internal waves can smooth the sea surface, and only fossil and zombie turbulence patches can radiate large-amplitude, near-vertical, internal waves. Where does all this dissipated energy come from? Extrapolating the measured levels of Fig. 7b to the large spectral anomaly surface areas of Fig. 1a (top) proves it cannot come

from the 50 kw of pumping power required to inject low salinity Sand Island wastewater from the diffuser into denser seawater at 70 m depths. If $\varepsilon \approx 10^{-5} \text{ m}^2 \text{ s}^{-3}$ shown in Fig. 7b is representative of the FTW and ZTW power vertically radiated and dissipated at the surface, then about 5 kw, or 10% of the 50 kw pumping power, is dissipated by breaking FTWs and ZTWs in a 50 m wide strip 10 m deep along the km length of the diffuser for a $5 \times 10^{-2} \text{ km}^2$ surface area. This is 100 kw km^{-2} .

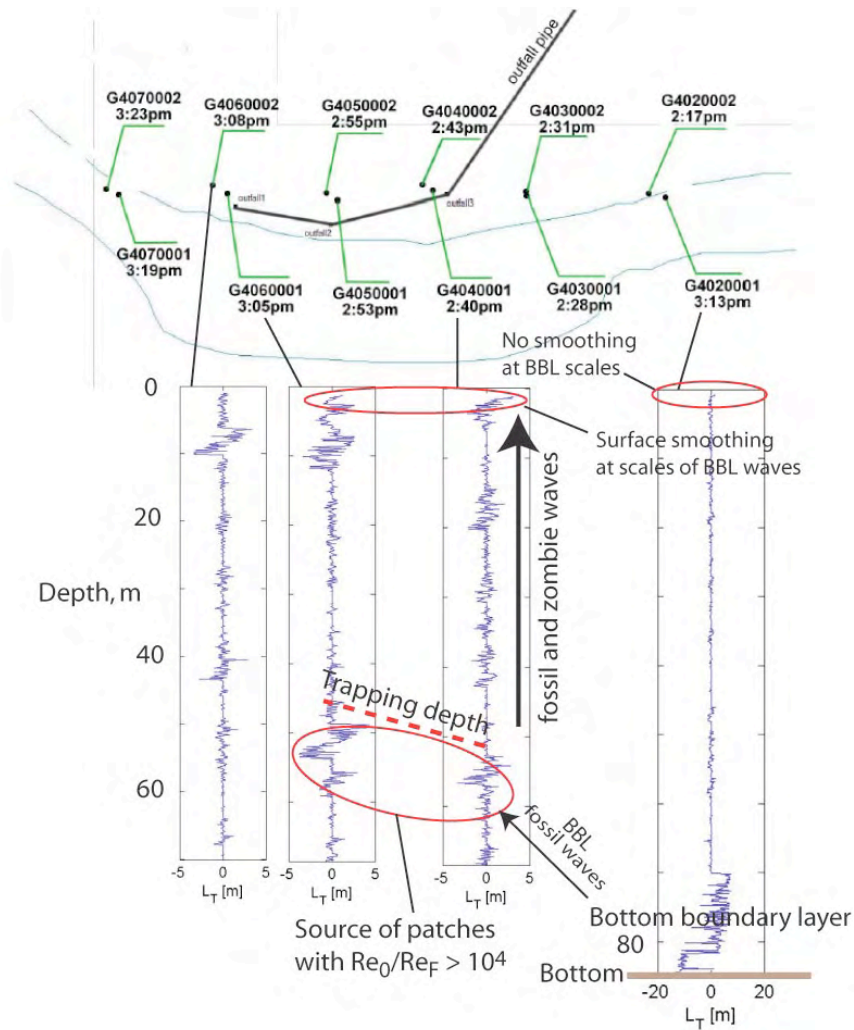


Figure 7a: Vertical profiling station locations in Mamala Bay Sept. 2, 2002, during the IKONOS satellite overflight. Profile G4060001 (shown in Figs. 8 and 12) is about 50 m to the NW of the end of the diffuser pipe reflecting the direction of the ship drift. Profile G4030002 about 600 m east of the diffuser sampled the weaker ambient patch H in the 5-10 m depth wind mixed surface layer compared with patches F and G, which show larger Re_0/Re_F values attributed to direct fossil turbulence wave breaking. Weak brightness anomaly fragment 81 (Fig. 3) NW of the diffuser pipe suggests that indirect BZTMA fossil wave breaking patterns contribute to the surface smoothing.

Thus the 200 km² area of the Fig. 4 (top) 9/13/2003 anomaly region, extrapolating the Fig. 7b results, requires 2 megawatts of surface smoothing to power the remote detection of submerged turbulence for this experiment, far more than available from the outfall itself. The BZTMA mechanism provides a means of extracting the large power levels apparently required for the satellite detections of submerged outfall fossil turbulence from ambient soliton-like internal waves, as shown by RASP, Fig. 1a (top).

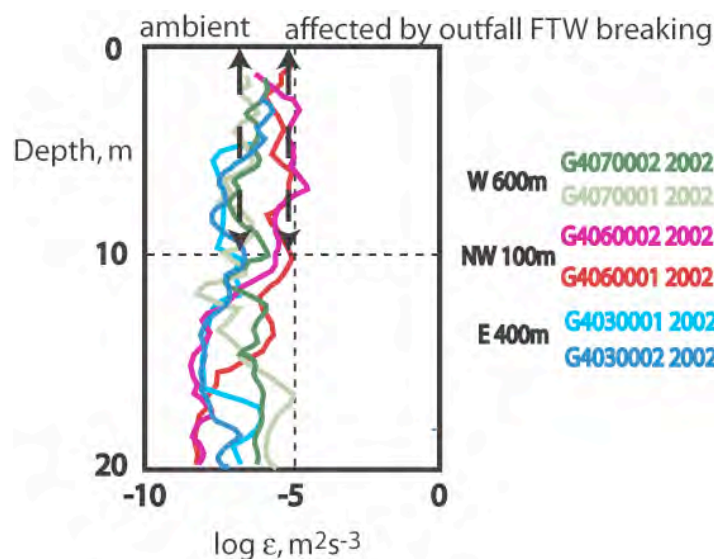


Figure 7b: Near surface dissipation rates are increased by outfall fossil turbulence waves near the end of the diffuser by two orders of magnitude above ambient values east and west of the outfall. Station locations and times are shown in Fig. 7a. No surface manifestations of the outfall (as in Fig. 1b) were observed.

Boguki et al. (1997) estimate that 73% of coastal internal wave energy is carried by ISWs, which they show are effective at coastal bottom re-suspension and mixing. What fraction of this energy is extracted from the ISWs and beamed vertically by the BZTMA mechanism? What fraction of the turbulent kinetic energy created by tides and currents on the ocean bottom finds its way to the surface by vertical maser-action beaming of FTWs and ZTWs?

Figure 8 (top) shows mean and microstructure profiles from station G4060001 located about 50 m to the west of the end of the diffuser pipe, reflecting the ship drift due to the surface currents and wind in this direction. Clearly the waste field has also been advected by the current and horizontal diffusion as shown by the low salinity and high turbidity regions between 42 and 50 meters, which we interpret as the wastewater trapping depth.

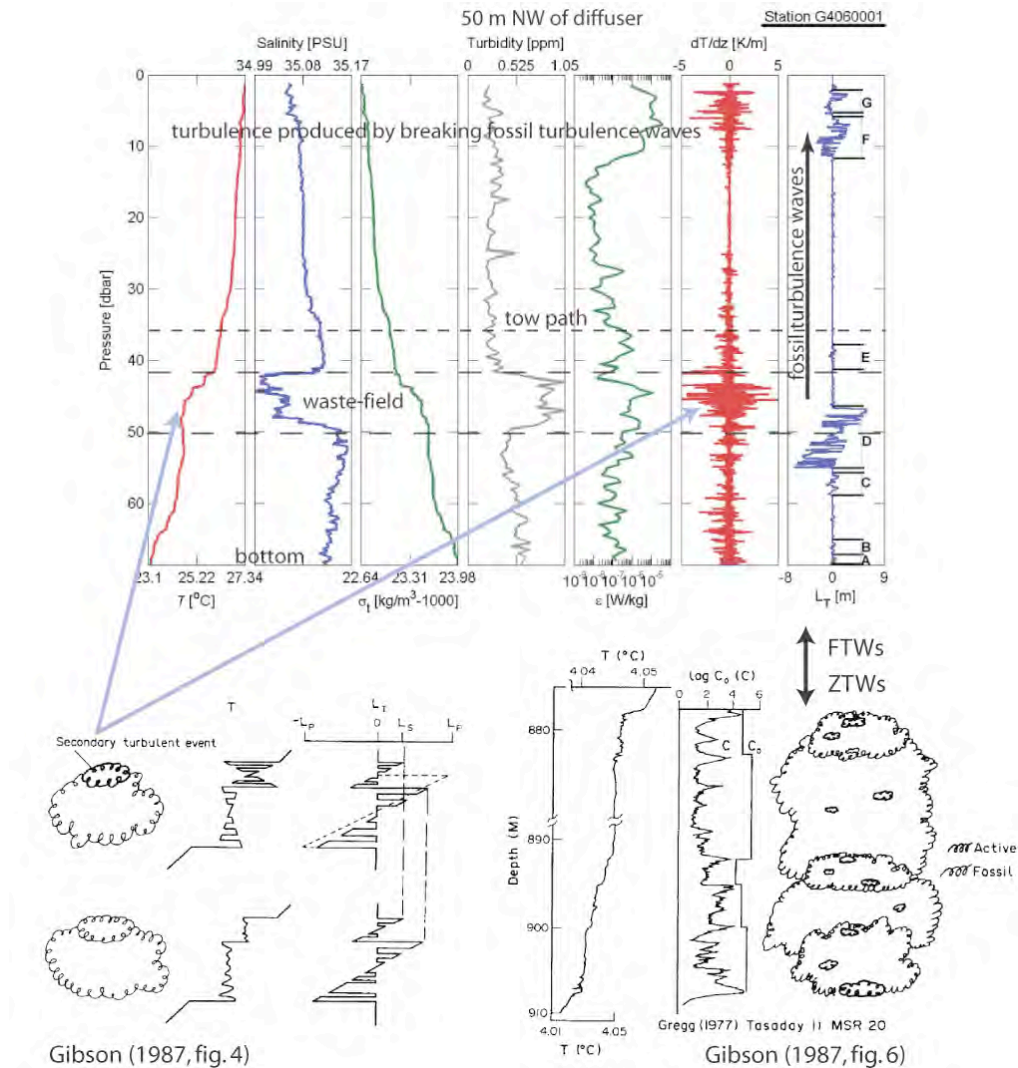


Figure 8: (top) MSS dropsonde profiles at station G4060001 50 m NW of the diffuser pipe end. The buoyancy trapped wastewater plume at 42-51 m is identified by cool, low salinity, turbid water with large temperature gradients. The MSS tow path at 36 m depth samples temperature mixing (Fig. 16) triggered by radiated fossil turbulence waves from the waste-field. Thorpe overturn scales (Thorpe, 1977) of the microstructure patches increase as the buoyancy driven turbulence rises and cascades to larger scales. The largest L_T values are at the trapping depth in patch D. Large values are also found in the 3-10 m depth range in patches F and G, where fossil turbulence waves break at the base of the wind mixed layer. The strong temperature microstructure region above patch D is a secondary turbulence event that has radiated its energy vertically as FTWs, (bottom left) as explained by Gibson (1987, fig. 4). (bottom right) The most active microstructure region reported by Gregg (1977) indicates a primary and several secondary fossil turbulence events producing the FTWs and ZTWs of BZTMA, Gibson (1987, fig. 6).

Below the trapping depth both turbidity and temperature dissipation levels are above ambient values but less than trapping depth values. Viscous dissipation rates reach a maximum near $10^{-5} \text{ m}^2 \text{ s}^{-3}$ near the sea surface from indicated fossil turbulence wave breaking in patches F and G, one or two orders of magnitude above the ambient levels from wind mixing, as shown by profile G4020001 and Fig. 7b.

To detect anomalous levels of mixing due to breaking fossil turbulence waves caused by the submerged fossil turbulence field, an MSS instrument was towed 5-10 m above the waste-water trapping depth. The results are presented in the following (see Fig. 16). They support present interpretations from vertical profiling that enhanced mixing levels exist above the advected wastefield due to FTWs and ZTWs breaking as they propagate near-vertically through the stratified water column on their way to the surface.

Figure 8 (bottom) shows the Gibson (1987, figs. 4 and 6) analysis of BZTMA physical processes and the most active microstructure region presented by Gregg (1977ab) from profiles 900 m deep in the north Pacific. From the Gibson (1987) analysis, the step structures in temperature with large temperature dissipation rates but negligible Thorpe overturning scales above patch D, Fig. 8 (top) are fossils of a secondary turbulence event that has radiated its ZTW energy near vertically to the surface. Cox numbers of secondary turbulence events approach Cox numbers of the primary event at beginning of fossilization, Gibson (1987, eq. 20). This analysis justifies the semi-empirical $+1/3$ slope of zombie turbulence recovery on hydrodynamic phase diagrams presented by KBG, and in Figs. 12, 13 and 14 below, opposite to the $-1/3$ slope for fossil turbulence decay, Gibson (1986).

Figure 9 shows mean and microstructure profiles from a station about 3 km south of the diffuser on the western edge of the SE brightness anomaly lobe. The largest Thorpe overturn scale patch L is at approximately the diffuser depth of 70 m (HPD locations of the patches in this profile are shown in Fig. 12). Temperature fluctuations within patch L are smaller than ambient levels and a very large Re_0/Re_F value $\sim 10^5$ is found by $+1/3$ slope extrapolation, reflecting zombie turbulence processes where turbulence is generated at the patch boundaries by ambient internal waves that complete the interior mixing and increase the patch size and Thorpe overturn scale (as shown in Fig. 11 below). Patches IJK below, and patches MNOP near the sea surface in such a spectral anomaly region are likely candidates for mixing patches produced by zombie turbulence waves radiating near vertically by patches like L and IJK, pumped energy extracted from the ambient internal wave field vertically by maser action.

Figure 10 illustrates the effect of choosing different vertical separation distances ΔZ_{ave} for the computation of the effective ambient buoyancy forces available to damp turbulence in a growing turbulence patch. N^2 is shown in Fig. 10 for patch D of Fig. 8 (top), computed as a function of ΔZ_{ave} from the rearranged Thorpe density profile. The patch size L_p and the maximum Thorpe overturning scale $L_{T_{max}}$ are shown for comparison. A range of constant N^2 was found for ΔZ_{ave} between $L_{T_{max}}$ and $2L_{T_{max}}$. The maximum Thorpe overturning scale of about 6 m for outfall fossil turbulence patches shown in Fig. 10 is typical for the RASP 2002, 2003 and 2004 experiments.

Unambiguous identification of individual fossil or active turbulence patches sometimes requires care, Galbraith and Kelley (1996), Prandke and Stipps (1992). Use of multiple zero crossings of the vertical temperature gradient between patches is generally found to be the most computationally and physically robust method for isolating patches (Prandke, personal communication).

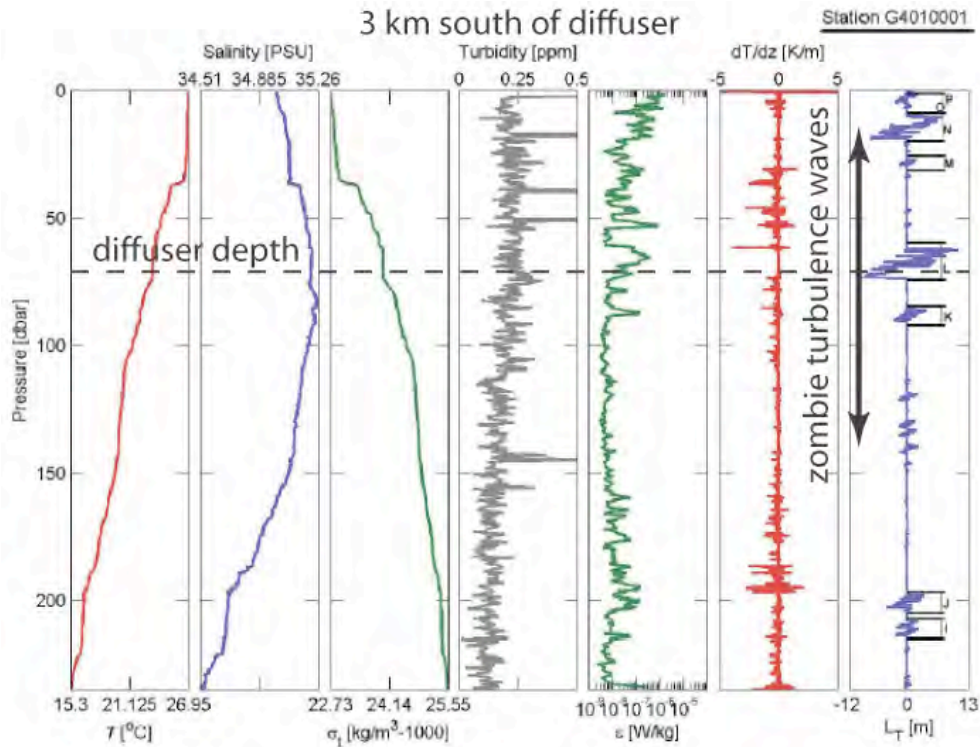


Figure 9: MSS dropsonde profiles at station G4010001 about 3 km south of the diffuser. The diffuser depth is shown by a dashed line. Patch L appears to be a 10 m L_{Tmax} fossil turbulence patch produced by the wastewater injection at 68-70 m and deeper than its trapping depth by about 20 m by the off shore advection. Its location near the base of the seasonal pycnocline and the spectral anomalies in fragments 14, 15 and 25 suggest that zombie turbulence radiation is reflected by surface patches M, N and O and deeper patches J and I below 200 m. HPD values for the patches shown in Fig. 12 suggest patch K also is an outfall fossil turbulence patch, with $Re_0/Re_F \sim 10,000$.

Figure 11 shows the evolution of an actively turbulent patch at beginning of its fossilization, with critical Froude number and length scale L_{R_0} , to an active-fossil hydrodynamic state (stages 1,2,3) and then as it is re-activated by ambient tilting to form a zombie turbulence patch (stages 3,4,5), Gibson (1987). The geometry of the fossil and zombie (top) and the dissipation rate of its turbulence are reflected on a

hydrodynamic phase diagram (bottom). Strong FTW radiation occurs after stage 1 and decreases as mechanical energy is lost from the patch by friction. The trajectory on a hydrodynamic phase diagram is a straight line with slope approximately 1/3 or slightly less. Tilting of the strong density gradients at top and bottom of the fossil (stage 3) by ambient internal waves results in vorticity production at a rate $\nabla\rho \times \nabla p / \rho^2$, where ρ is the density and p is the pressure, because the pressure gradient ∇p is always vertical and down. Turbulence will be produced if the tilting persists (red lines) and the fossil turbulence patch (stage 3) will be re-activated to fossil-zombie (stage 4) and fully zombie (stage 5) hydrodynamic states, along a straight line, with radiation near vertically of ZTWs, with slope again approximately 1/3 or less, taking the patch to regions of the HPD indicating larger Re_0/Re_F values than existed in the original patch.

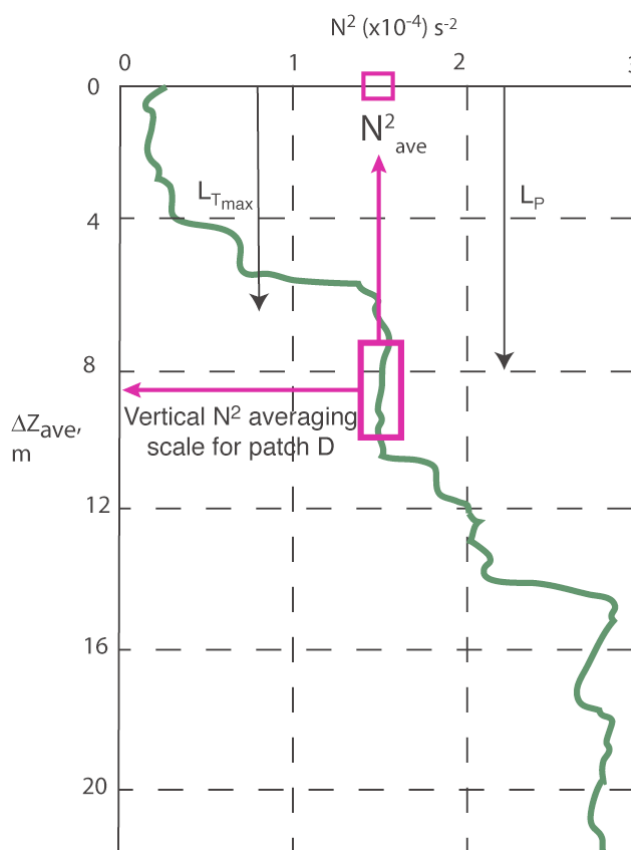


Figure 10: Stratification frequency N^2_{ave} computed as a function of vertical depth differences ΔZ_{ave} for the strongly fossilized patch D shown in Fig. 5 just below the wastewater trapping depth. A range of constant N is found for vertical averaging scales somewhat larger than the maximum Thorpe overturning scale L_{Tmax} and patch scale L_P , representing the ambient stratification preventing further growth of the turbulent patch.

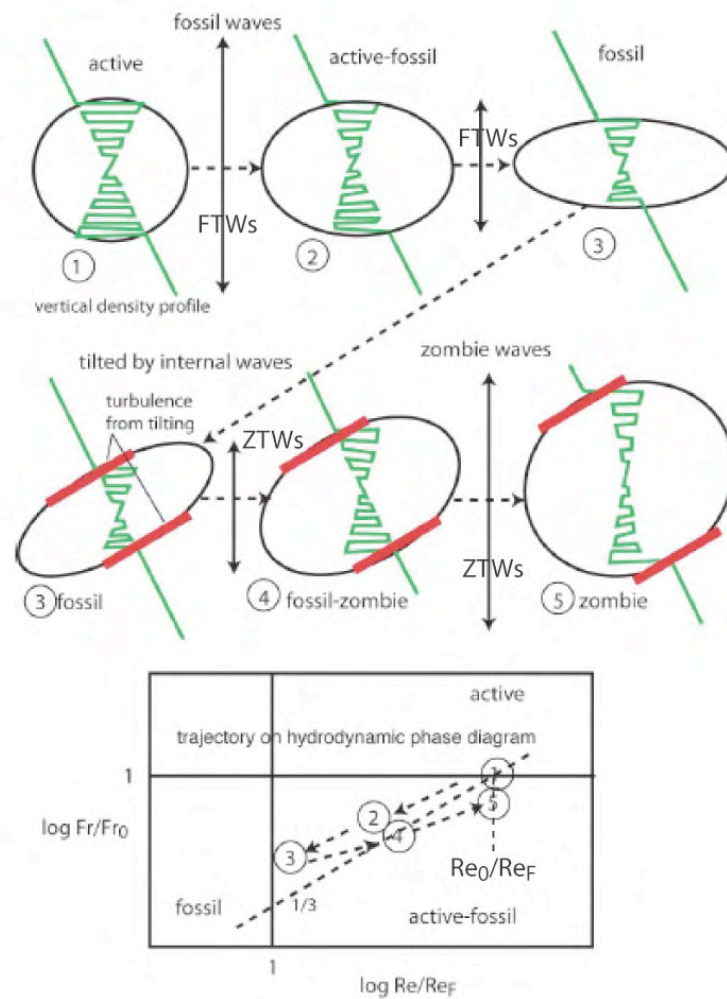


Figure 11: The physical mechanism of zombie turbulence patch formation from a fully turbulent microstructure patch at beginning of fossilization and its trajectory on a hydrodynamic phase diagram. Both the fossilization trajectory 1-2-3 and the zombie formation trajectory 3-4-5 should follow slightly less than $1/3$ slope paths on the log-log plot, Gibson (1987). Thus fossilized patches tend to underestimate Re_0/Re_F , and zombie turbulence patches can indicate large Re_0/Re_F values that never existed. Red lines indicate vorticity and turbulence formation from tilting of the fossilized patch by ambient internal waves and shears.

Hydrodynamic Phase Diagrams

Figure 12 shows the microstructure patches A-G of Figs. 8 (top) from station G4060001 50 m NW of the diffuser-pipe-end classified according to their hydrodynamic states on a hydrodynamic phase diagram (HPD) compared to ambient near surface conditions sampled 200-600 m east of the diffuser (triangle H) and patches I-J from profile G4010001 in the SE anomaly lobe region about 3 km south.

As shown in Fig. 10, to properly compute N for each patch it is important to select a vertical separation distance ΔZ_{ave} larger than the largest Thorpe displacement L_{Tmax} by a sufficient amount so that N_{ave} for the patch will represent the ambient stratification that opposed the inertial-vortex forces $\vec{v} \times \vec{\omega}$ of the growing eddies of the active turbulence in the patch before its fossilization.

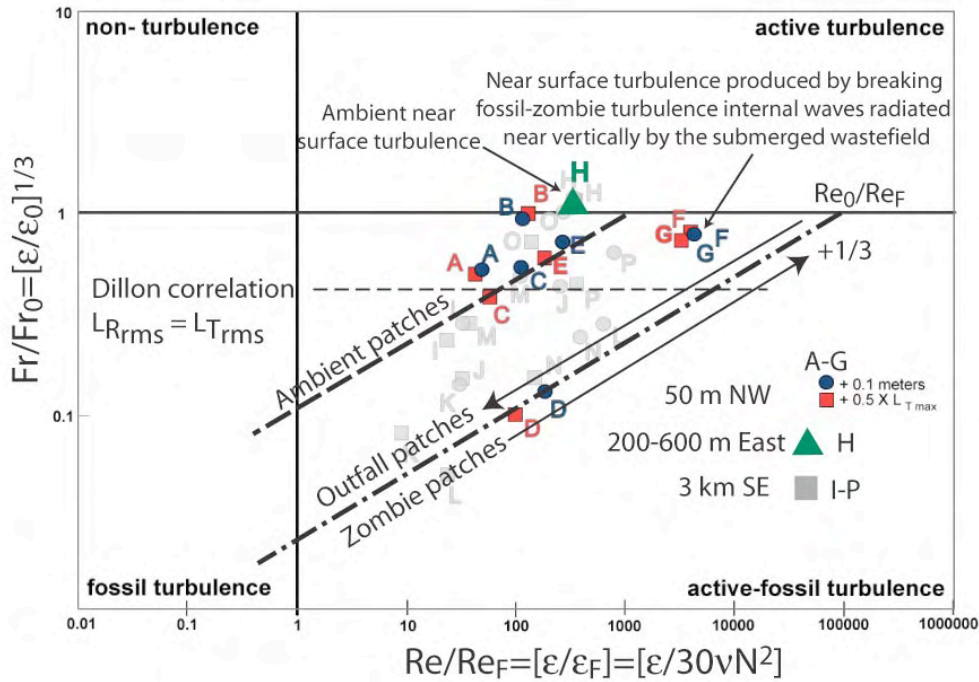


Figure 12: HPD points A-G are shown for the G4060001 dropsonde profiles of Fig. 8 about 50 m NW of the end of the diffuser. N is averaged over vertical scales 0.1 m larger (black circles) and $0.5 L_{Tmax}$ larger (red squares) than the patches. The Thorpe overturn scales increase from A to D as the buoyant turbulence of the plume cascades from small scales to large and then fossilizes. Dimmed patches I-P are from the station G4010001 profile of Fig. 9 in the SE surface brightness anomaly lobe of Fig. 3. Patches K and L extrapolate to large $Re_0/Re_F \sim 10^4$ values, indicating they are outfall fossils produced by the wastewater discharge.

Sensitivity to the vertical averaging scale $\Delta Z_{ave} = L_{Tmax} + 2\Delta z$ is shown in Fig. 12 by computing each hydrodynamic state for both $\Delta z = 0.1$ m (dark circles) and $0.5 L_{Tmax}$ (red squares) to bracket the range of reasonable values, as indicated by Fig. 10. Not much change results for these two choices except for the largest L_{Tmax} patches such as D and L.

A comparison is made in Fig. 12 to the Dillon (1982) correlation $L_{Rms} \approx L_{Trms}$ between root-mean-square Ozmidov and Thorpe overturning scales. This correlation is sometimes used as evidence that microstructure patches in the stratified ocean are

never fossilized but are always in a state of continuous turbulent equilibrium, Caldwell (1983), Dillon (1982, 1984), Gregg (1987), so that the average viscous dissipation rate for the oceanic region or layer can be estimated by averaging Thorpe overturning scales; for example, Galbraith and Kelly (1996), Alford et al. (2006), Rudnick et al. (2003), Baumert et al. (2005).

No correlation of L_T and L_R is indicated by the present data for individual patches. The underlying concept of the Dillon method; namely, that the fossil turbulence process does not exist, neglects the important property of stratified turbulence that the largest most powerful turbulent events that dominate average mixing rates and vertical diffusion are also the most intermittent in space and time and most difficult to sample, Baker and Gibson (1987). Most of the mixing and vertical diffusion in the ocean occurs in large fossilized microstructure patches that persist thousands of times longer than their original patches in actively turbulent states.

To avoid under sampling errors, microstructure data sets should be evaluated for adequacy using HPDs to detect the dominant turbulence events in the region. In extremely intermittent layers and regions of the ocean, undersampling errors can be quantitative, qualitative, and vast, due to intermittency effects, Gibson (1983, 1987, 1991abc, 1999). HPD classifications of microstructure patches such as Fig. 12 permit the detection of the dominant turbulent events in a region of the ocean by extrapolation along the $-1/3$ locus of fossilization and $+1/3$ locus for zombie turbulence formation (Fig. 11) to estimate the power of the original turbulence event, as measured by the ratio $\varepsilon_0/\varepsilon_F = Re_0/Re_F$.

As indicated in Fig. 12, patches A, B, and C below the trapping depth of the wastewater plume have relatively small values of Re_0/Re_F near 3000, only ~ 3 times larger than ambient turbulent patches and 10 times smaller than $Re_0/Re_F \approx 30,000$ of outfall fossil turbulence at the trapping depth. Because the fossilization time $t_{fossilization} \leq N^{-1}$, a single microstructure profile is unlikely to capture any of the dominant turbulence events in their original fully turbulent states, even when the profile is at the source of the events as for the near-outfall profile of Fig. 8 (top). Patch D is identified as a zombie-turbulence patch because the extrapolated $Re_0/Re_F \approx 100,000$ is larger than 30,000 determined in Fig. 14 as the Re_0/Re_F value for dominant outfall turbulence patches. The strong mixing region above patch D was identified as secondary (zombie) fossil turbulence in the discussion of Fig. 8 (top) and Fig. 8 (bottom) above.

Figure 13 shows a collection of all the HPD points for the trapping depth interval 40-60 m Aug. 28-29, 2002, classified according to their separation from the diffuser pipe. Those **close** to the diffuser pipe position (< 100 m - green squares) include two patches in the fully turbulent quadrant and but no active patches along the decay line extrapolating to maximum Re_0/Re_F values of order 10^4 . Therefore it appears from Fig. 13 that the dominant turbulent mixing patches at trapping depths have been under sampled. All such patches at **near** distances ~ 600 m (red circles) are strongly fossilized except for one actively turbulent patch with $Re_0/Re_F < 100$. **Far** patches beyond 3 km at 40-60 m depths all have Re_0/Re_F values less than 10^3 , which we take to be the ambient maximum for this depth. More samples are required to detect fully

turbulent, or even fossilized, outfall turbulence patches; that is, those patches reflecting Re_0/Re_F values of 25,000 characteristic of the diffuser wastewater at trapping depths. Because such patches were not detected, the outfall turbulence trapping and fossilization process has been under sampled by the Aug. 28-29, 2002, data set. Patches were identified by the method of zero crossings, Prandke and Stips (1992), where several adjacent zero vertical temperature gradients are required as the criterion to separate patches.

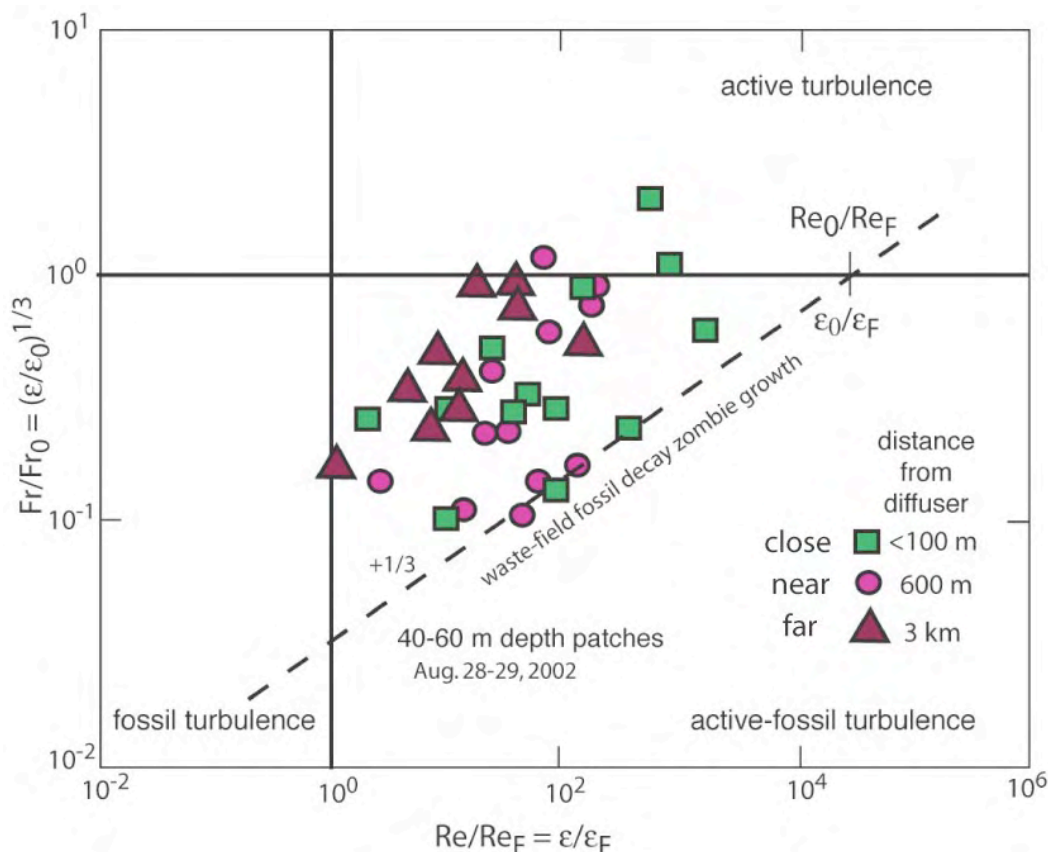


Figure 13: Hydrodynamic phase diagram for 40-60 m depth range microstructure points, **close** (< 100 m, 6 profiles, squares), **near** (~600 m, 6 profiles, circles) and **far** (~3 km, 3 profiles, triangles) from the diffuser pipe (Aug. 28-29, 2002). The dashed line with slope +1/3 shows the locus expected for decaying fossil turbulence patches and their re-activated “zombie” descendants. Patches **close** and **near** the diffuser pipe have large extrapolated Re_0/Re_F values $> 10^4$, larger than **far** patches with $Re_0/Re_F < 10^3$. More **close** patches had large Re_0/Re_F values and were actively turbulent than **near** patches. Neither **close** nor **near** categories showed active patches with $Re_0/Re_F > 10^4$, indicating that the dominant mixing process has been under sampled at both locations. Similarly the **far** category had no active patches with $Re_0/Re_F > 10^3$ and is therefore also undersampled.

Figure 14 shows 2618 HPD points for microstructure patches detected in various locations during the RASP 2003 experiments. In the region of the outfall with many anomalies, a few patches were found with a +1/3 slope extrapolation pointing to Re_0/Re_F of 30,000 for the most powerful outfall patches at the trapping depth just below the pycnocline (red triangles, upper left). Only three patches were detected in their completely actively turbulent state. Clear evidence of zombie (secondary) fossil turbulence formation is shown by patches indicating false large values of their initial normalized Reynolds number $Re_0/Re_F \sim 10^5$.

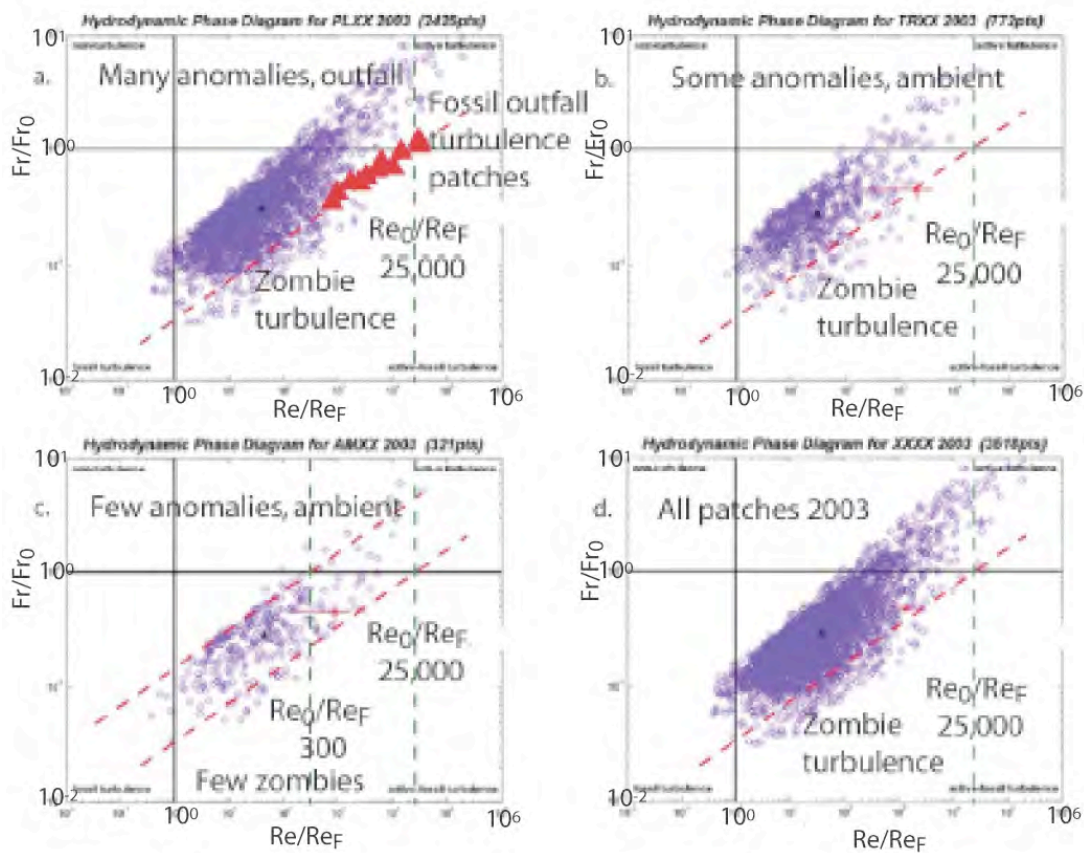


Figure 14: Hydrodynamic phase diagrams of 2618 patches from vertical profiles of RASP 2003. Only a few patches observed near the outfall in anomaly regions indicate a hydrodynamic state of active or nearly active turbulence (red triangle points upper left). This shows how rapidly stratified turbulence fossilizes and the dangers of undersampling this intermittent hydrodynamic state. Ambient regions have fewer outfall patches and fewer zombie turbulence patches.

Calculations from RASP 2004 from more than 10^4 HPD patches to greater depths (extending to the bottom) reveal a few patches with Re_0/Re_F values up to 10^6 by the +1/3 slope extrapolation method. None were in their actively turbulent state. Such

powerful events are difficult to sample directly because of their extreme intermittency. At fossilization such events can produce the 220 m wavelength ISWs detected in RASP by the FTW wave mechanism ($\epsilon_0 = 10^{-2} \text{ m}^2 \text{ s}^{-3}$, $N = 5 \times 10^{-3} \text{ s}^{-1}$, $L_{R_0} = 282 \text{ m}$). These ISWs may also be lee waves. It is a question for future research to determine how the soliton-like waves measured on the pycnocline, and responsible for the numerous RASP detections of submerged outfall fossil turbulence, are produced. From their random directions, they do not seem to be radiated by the outfall, but this hypothesis should also be confirmed.

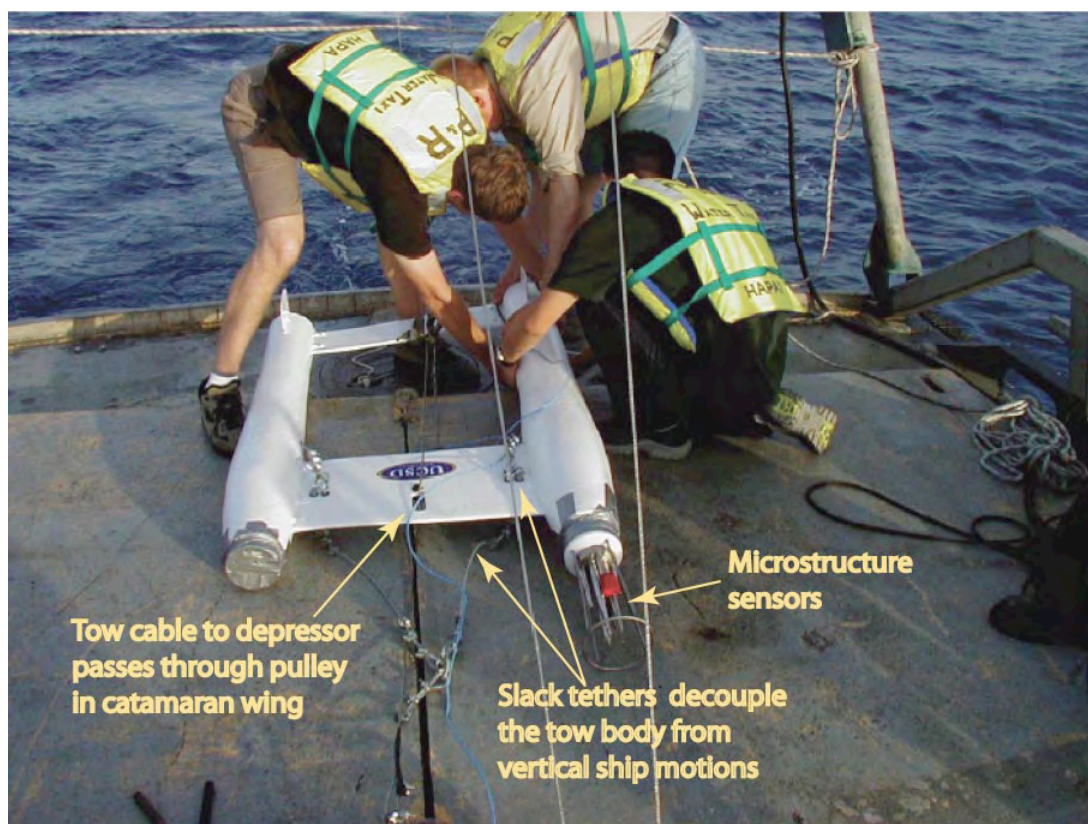


Figure 15: Catamaran tow body. The tow cable passes through a pulley in the wing to a depressor that keeps the cable near vertical. Slack tethers from the depressor below and the tow cable above are yoked to attachment points on the forward wing aligned with the pulley. The MSS microstructure system is mounted in the port catamaran hull with an electrical cable to the ship. Attending the fish on the HAPA deck are Pak Tao Leung, Hartmut Prandke, and Fabian Wolk.

Horizontal Microstructure Profiles

A catamaran tow body was constructed to decouple vertical ship motions. The MSS sensor package is housed in the port hull, as shown in Figure 15. A tow cable passes through the forward wing and a pulley to the 20 kg aluminum hydrodynamic

depressor. The depressor keeps the tow cable nearly vertical near its end so the fish can fly above it. This method of decoupling is compared to other techniques in Nasmyth (1980).

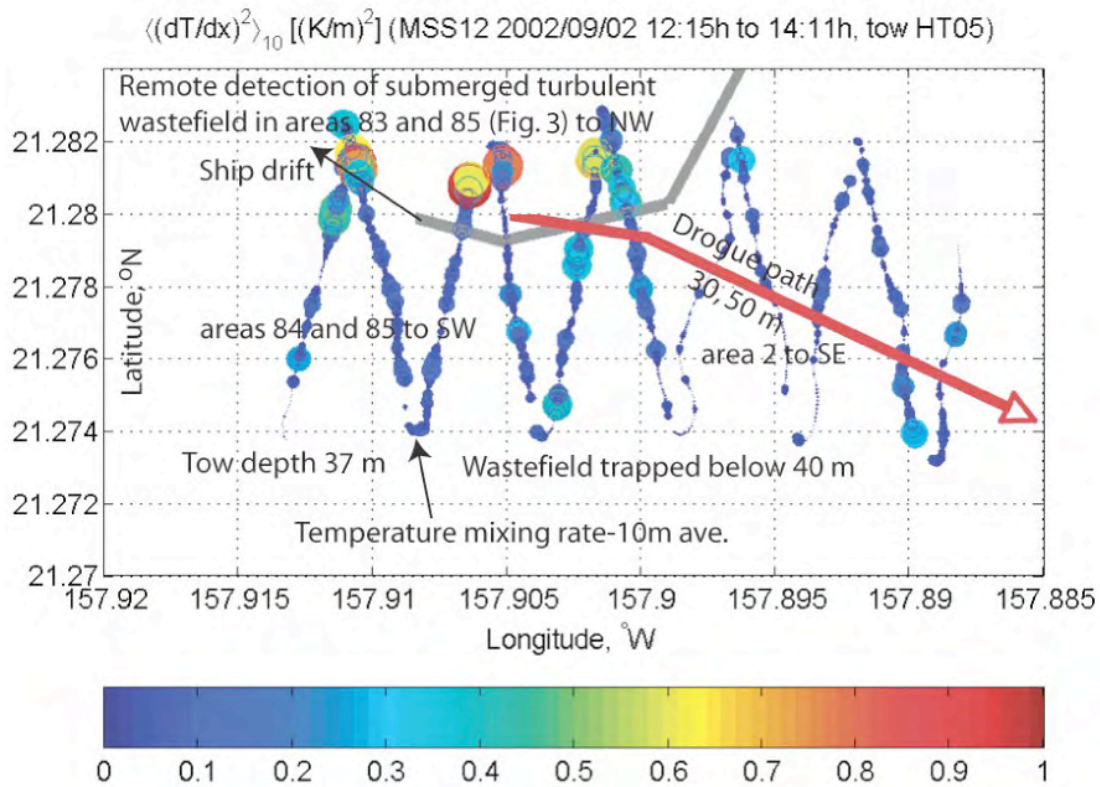


Figure 16: Circle sizes and colors indicate 10-m average temperature mixing rates along the 37 m depth tow path Sept. 2, 2002, 10 meters above the average trapping depth (Keeler et al. 2005). Regions of enhanced temperature mixing match areas of quasimonochromatic spectral anomaly detection of the outfall from the Ikonos-2 image, Bondur and Filatov (2003), in Fig. 3 a.

The pulley transmits horizontal forces. Vertical forces are transmitted by two slack tethers yoked to attachment points in line with the pulley on the wing above and below. The tethers serve as hydroelastic springs that gently transmit vertical ship forces under way, and permit retrieval. The forward wing resists vertical motions. The aft wing resists pitch, and the tail fins resist yaw. Tow speeds were typically 2 m s^{-1} , and ranged between 0.5 and 3 m s^{-1} . Signals from the MSS instrument were transmitted to the ship for recording and monitoring in the ship laboratory by a signal cable attached by plastic tie wraps to the stainless steel upper tether and tow cable during deployment.

Figure 16 shows ten meter averaged temperature mixing rates along a zigzag towpath over the diffuser at 37 m depth to place the MSS sensors just above the wastewater trapping depth of 42-50 meters. The purpose was to detect further evidence of enhanced turbulent mixing due to FTW and ZTW vertical radiation and breaking.

Further evidence of enhanced mixing above the wastefield by FTWs and ZTWs is shown in the horizontal profile of Fig. 16. Near surface advection of the wastefield to the NW was apparent from the ship drift during vertical profiling, as shown by the black arrow at the end of the diffuser, and by vertical microstructure stations G4060001 and G4060002 of Figs. 7ab and 8. The west component of ship drift reflects steady 10-14 knot winds from the east, and the north component possibly compensates for off shore SE advection shown by the 30 m and 50 m drogue path (red arrow).

The strongest mixing at the 35 m tow depth of Fig. 16 is to the NW of the outfall diffuser pipe, which may reflect a NW advection by currents of FTWs and ZTWs as they propagate toward the surface.

Regions of enhanced mixing in Fig. 16 are in the same SW and SE lobed pattern of the spectral anomaly fragments 84 and 85 to the SW, fragment 2 to the SE, and fragment 83 and 85 to the NW from the spectral anomaly map area numbers of Fig. 3.

Discussion of Results

Hydrodynamic phase diagrams in Figs. 12, 13 and 14 for thousands of microstructure patches measured at all locations in Mamala Bay show clear evidence of fossil turbulence patch formation after the inertial-vortex-force driven turbulence growth in the stratified fluid from small scales to large, as well as zombie turbulence patch formation as described in Fig. 11. Active turbulence patches with Thorpe overturning scales that grow as the turbulence evolves were found in the buoyant turbulent wastewater plume, Fig. 8 (top), with strongly fossilized patches near the buoyancy trapping depth at the diffuser and at distances up to 7 km with Re_0/Re_F ratio $\sim 30,000$, Figs. 12, 13, 14. Patches in the trapping depth range caused by the waste-water discharge were detected 600 m from the diffuser with the same Re_0/Re_F ratio $>10^4$ as detected <100 m from the diffuser pipe location but with Re/Re_F values <100 compared to $Re/Re_F \sim 1000$ for distances <100 m, Fig. 13. If fossil density turbulence patches exist with significant fossil-vorticity-turbulence energy, then fossil turbulence waves can be radiated in the near vertical direction. Additional vorticity and energy for vertical radiation and mixing can be absorbed from ambient internal wave motions by the zombie turbulence mechanism, Fig. 11, giving the beamed zombie turbulence maser action radiation of energy and information to the surface and the observed surface brightness anomalies of Figs. 1b (top), 2, 3, 4 (top), and 5.

Does evidence exist of FTWs elsewhere in the ocean? Dropsonde profiling of Thorpe overturning scales were carried out over the Romanche Fracture Zone (RFZ), one of the channels for the powerful flow of Antarctic bottom water through the Mid-Atlantic Ridge with regions of very rough bottom topography. Polzin et al. (1997) and Ferron et al. (1998) report RFZ measurements of ϵ and L_T all the way to the

bottom at depths more than 5 km. Large L_T values detected in the water column appear vertically connected to the most powerful regions of topographically generated turbulence, and 1-2 km above. Are these mixing regions created by FTWs radiated near-vertically from the measured topographic turbulence regions of the RFZ? Do the patches show evidence of secondary turbulence events, as shown by Gibson (1987), Fig. 8 (bottom)? SAR images such as that of Fig. 1c (bottom) showing evidence of bottom topography FTWs in the North Atlantic do not yet seem to be available from the South Atlantic.

Vertical sampling of oceanic microstructure gives high signal to noise but is subject to under sampling errors from extreme intermittency in space and time of the oceanic turbulent mixing process. The deep dark mixing paradox of the > 2 km deep main thermocline is the result of such under sampling errors, Gibson (1991c). Vertical eddy diffusivities indicated by the smoothed vertical temperature gradient are least $10^{-4} \text{ m}^2 \text{ s}^{-1}$, Munk (1966), Munk and Wunsch (1998), compared to inferred values from vertical microstructure sampling 30 times smaller, ignoring evidence that the dominant patches were strongly fossilized, Gibson (1987). The deep dark mixing paradox is resolved by recognizing that turbulent mixing in the thermocline below 2 km is extremely intermittent, with viscous dissipation rate ϵ and temperature mixing rate χ well described by intermittent lognormal probability density functions, Baker and Gibson (1987).

Intermittency factors I_ϵ and I_χ are variances of the natural logarithms of these dissipation rates, and the mean to mode ratio of a lognormal random variable $\exp(3I/2)$ is a good measure of the undersampling error because sparse samples such as dropsonde measurements of ϵ and χ are measures of the mode whereas the mean ϵ and χ are measures of the vertical diffusivity and may be larger than the mode by factors of $\exp(3I/2)$. Because I_ϵ and I_χ increase from 3 to 7 as latitude decreases from mid-latitudes toward zero at the equator where the range of turbulence mixing is maximum, the undersampling error increases from about a factor of 90 to a factor of 36,000. Neglecting fossil turbulence evidence and the effects of intermittency may cause not only quantitative but qualitative undersampling errors, where regions with maximum average dissipation rates, mixing and vertical diffusion could be identified as regions with minima in these important turbulent quantities.

Evidence indicates that the largest outfall fossil turbulence mixing patches that dominate the RASP 2002 remote detection process were under sampled. Fig. 12 provides HPD points for the Sept. 2, 2002, satellite over flight, and Fig. 13 provides HPD points from profiles taken Aug. 28-29, 2002, at the 40-60 m trapping depth range, and at distances **close**, **near** and **far** from the diffuser. Neither of these HPD plots revealed patches with Re/Re_F near 30,000 as expected from extrapolated Re_0/Re_F . Adequate sampling of the outfall microstructure requires that HPD patches must be detected in the active-turbulence quadrant, with Re/Re_F values as large as the largest extrapolated Re_0/Re_F inferred in these categories from the fossilized patches. If the outfall diffuser produces the dominant turbulence events of Mamala Bay, only **close** active turbulence patches with Re/Re_F near 30,000 should be found.

Thousands of patches in the RASP 2003 results were required to support this expectation, as shown in Fig. 14.

Numerical simulations and laboratory experiments show strong coupling between turbulence in contact with stratified fluid, Sutherland and Linden (1998). We suggest their radiated narrow-frequency-band waves are small amplitude fossil turbulence waves that reflect the Ozmidov scale of turbulence at fossilization L_{R_0} . Both soliton waves and outfall fossil turbulence patches are trapped on the deep seasonal pycnocline, as observed in Mamala Bay for the present experiments. This permits the remote sensing of submerged turbulence by large scale patterns of the solitons radiated to the surface by ZTWs of the BZTMA mechanism, described in Fig. 1d (bcd). Direct radiation of internal waves to distances of 20 km with sufficient energy to have detectable surface effects is very unlikely, as shown in GBKL.

At the outfall trapping depth, inertial-vortex-forces $\vec{v} \times \vec{\omega}$ of turbulence as it cascades to larger scales are damped at the Ozmidov scale at beginning of fossilization $L_{R_0} \equiv (\varepsilon_0 / N^3)^{1/2}$ by buoyancy forces of the ambient stratification $N = [-g(\partial\rho/\partial z)/\rho]^{1/2}$, where \vec{v} is velocity, $\vec{\omega}$ is vorticity, g is gravity, ε is the viscous dissipation rate and z is up. Damping turbulence by stable stratification produces a unique class of internal waves termed fossil-vorticity-turbulence (FVT) that is also a class of fossil turbulence, Gibson (1980), Gibson (1999), Leung and Gibson (2004), Gibson (2004). FVT internal waves are saturated and retain most the kinetic energy of the turbulence at scales near L_{R_0} , Gibson (1986, 1987). They bob at the local stratification frequency N but do not propagate and do not overturn. Overturning microstructure for various hydrophysical fields (temperature, salinity, density, vorticity) produced by turbulence become fossil turbulence first at the largest scales L_{R_0} and then at smaller scales as L_R decreases toward the scale of complete fossilization $L_{RF} = (30\nu/N)^{1/2}$, where $\varepsilon_F = 30\nu N^2$ is the dissipation rate at complete fossilization.

Fossil turbulence patches do not collapse as sometimes assumed, but retain information about their largest previous dissipation rate ε_0 in the maximum Thorpe overturning scale from the relation $L_{T\max} = 0.6L_{R_0}$, Gibson (1987). This is the physical basis of the Dillon correlation $0.8(L_T)_{rms} = L_R$, Dillon (1982), which is not a reliable estimator of ε_{ave} , from the intermittency of ε as discussed, and is not evidence that fossil turbulence does not exist as Dillon (1982, 1984) and Caldwell (1983) suggest.

FVT wave motions are reduced by friction and then couple to the ambient stratification and radiate fossil-turbulence-waves (FTWs) nearly vertically (40° - 50°) in a narrow wavenumber range $\lambda_{FTW} \cong L_{R_0}$. Small amplitude internal waves are reflected by stratified layers and shear layers but large amplitude FTWs produce turbulent patches as they tunnel through weakly stratified regions, Sutherland and Yewchuk (2004), with some fraction of their energy captured on bounding strongly stratified layers to produce secondary turbulence, as well as horizontally-propagating narrow-frequency-band L_{R_0} scale ISWs.

KBG propose that $\lambda_{FTW} \cong L_{R_0}$ for FTWs explains the narrow spatial-frequency band signature of internal waves radiated by turbulence in contact with a stably stratified fluid as observed in the laboratory, Dohan and Sutherland (2003), Sutherland and Linden (1998), Sutherland et al. (1999). KBG term such internal waves Linden-Sutherland waves (LSWs), Fig. 1d (d).

FTWs are large amplitude LSWs that can only be produced by turbulence as it fossilizes. Small amplitude LSWs can be produced without turbulence in the laboratory by a moving sinusoidal boundary, Aguilar et al. (2005). Figure 1c (top) is a schematic representation of the RASP experiments and remote detection by the beamed zombie turbulence maser action (BZTMA) mechanism where outfall fossils produce ZTWs by extracting energy and wavelength information from quasimonochromatic ISWs.

The photograph in Fig. 1c (top) of the sea surface from the ship positioned above the west end of the outfall shows surface smoothing by FTWs and ZTWs about 50 m to the NW. Surface waters had no discoloration or smell and microstructure profiles showed turbulence and fossil turbulence patches were not vertically continuous below the smoothed surface. The turbulent waste field was therefore completely trapped by the stable stratification except for the near-vertical FTW and ZTW internal wave radiation from the submerged turbulence.

Laboratory studies of Linden (1975) show that up to 50% of the mechanical energy used by turbulence to deepen a mixing layer above stably stratified fluid is radiated at near-vertical angles ($\sim 45^\circ$) by narrow spatial-frequency band internal waves. In the ocean, powerful bottom boundary layer events with large L_{R_0} values in the 30-250 m range detected during the RASP experiments occur intermittently, with FTWs radiated near vertically and deflected horizontally when pycnoclines trap some fraction of their energy remaining from breaking events on the way to the surface.

In coastal waters near continental shelves, tidal lee waves seem a possible source of such ISWs although tidal FTWs from the bottom are not ruled out. Internal wave dispersion on the pycnocline narrows the spatial frequency band to the largest, most energetic scales to produce solitons, whatever the source of soliton energy. Slicks associated with such soliton waves occur at their trailing edge, LaFond (1962), where fossil turbulence can radiate FTWs. Secondary FTWs from fossil turbulence patches (ZTWs) in the water column provide a mechanism to move information revealing submerged turbulence events to the sea surface, taking advantage of the narrow frequency bands of much larger scale, and therefore more detectable, FTWs originating from powerful bottom boundary layer events.

Because FTWs have relatively large amplitudes near the breaking limit, they can easily be triggered to break by variations of shear and stratification in the water column, Sutherland (2001). If the source of FTWs is bottom topography with variable currents and tides, the FTW wave radiation can beam along paths of previous radiation to form mixing chimneys, analogous to amplified radiation beams formed in astrophysical masers, Alcock and Ross (1985ab, 1986). Fossil turbulence patches from previous FTW radiation can extract vorticity and turbulent kinetic energy from subsequent FTWs along a beaming channel to produce larger, reactivated fossil turbulence patches (zombie turbulence) in BZTMA mixing chimneys. Evidence of

BZTMA mixing chimneys from RASP 2003 is discussed in GBKL. This nonlinear beaming further complicates the vertical sampling process. Dissipation rates cannot be reliably estimated over topography in the deep ocean or at equatorial latitudes by the Dillon correlation without testing for intermittency effects from fossil turbulence theory and HPD sampling. The Dillon correlation method is used in the Hawaiian-ocean-mixing (HOME) collaboration, Rudnick et al. (2003), and the CARTUM Project, Baumert et al. (2005), without HDP sampling or any other tests of fossil turbulence parameters for intermittency effects on estimated mean values. Extreme quantitative undersampling errors, and even qualitative undersampling errors (e.g.: estimating minima where maxima exist) in mean dissipation rate estimates can easily occur at equatorial latitudes where intermittency effects are maximal. Strong turbulence and turbulent mixing are indicated by the equatorial maximum in biological activity, contradicting claims that equatorial mean dissipation rates are minimal and near laminar values, Gregg et al. (2003).

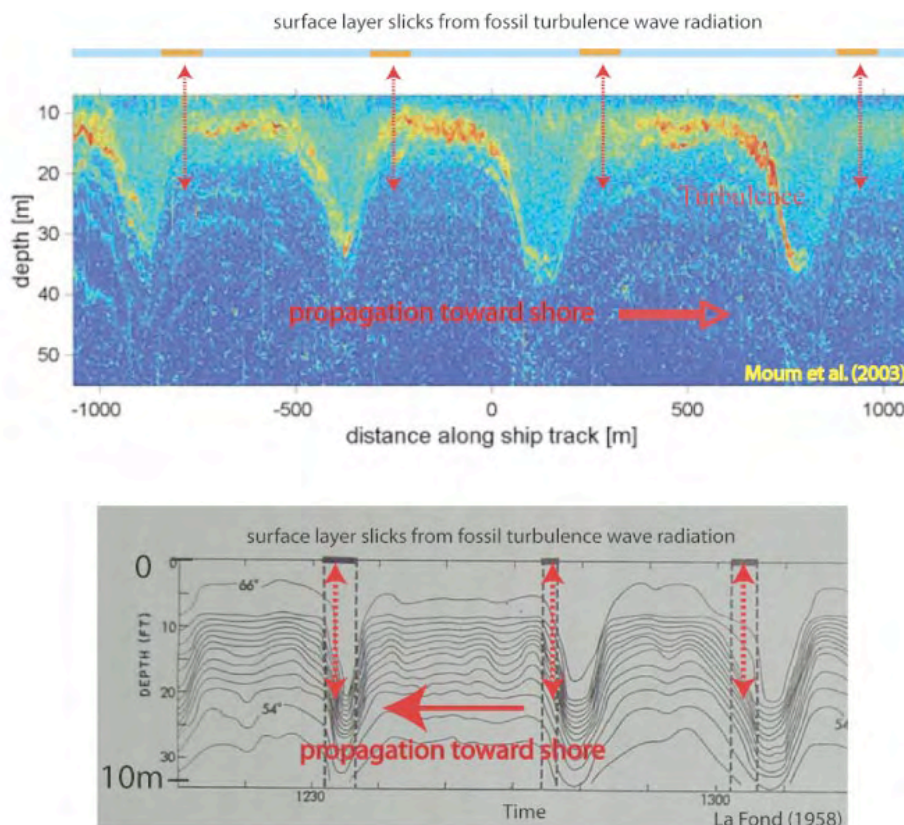


Figure 17: Examples of surface slicks and internal waves propagating toward shore on shallow thermoclines. The location of most slicks at the trailing edge of wave crests determined by LaFond (1962) July 12, 1958, in San Diego by time lapse photography and isotherm followers coincides with the likely locations of fossil turbulence and fossil turbulence waves (red dashed arrows) producing the slicks observed by Moum et al. (2003) off the Oregon coast.

Figure 17 shows internal waves and surface slicks propagating toward shore on shallow pycnoclines, as described by LaFond (1962) and Moum et al. (2003). The San Diego wave packets (bottom) occur intermittently about 10% of the time and are correlated with tides, suggesting their source is either lee waves or topographic-tidal-current turbulent events as shown in Fig. 1c(b, c). Wavelengths are 200-300 m (San Diego) and 500 m (Oregon). Slick formation occurs at the trailing edge of the advancing waves from the San Diego time-lapse photography and isotherm follower methods, coinciding with the likely location of large fossil turbulence patches and near-vertical radiation of FTWs (red dashed arrows) from the Moum et al. (2003) observations of turbulence along the waves.

Diamessis et al. (2005) have shown by numerical simulation that internal waves are radiated at 45° from a fossilized turbulence wake of sphere at the scale of the wake, which supports our assumption that $\lambda_{FTW} \approx L_{R_0} \approx L_{T_{max}}$, where $L_{T_{max}}$ is the maximum Thorpe overturn scale for the patch, Figure 18.

Conclusions

Submerged turbulence and fossil turbulence from the Sand Island Honolulu wastewater outfall has been repeatedly detected in RASP 2002, 2003, and 2004 from optical satellite images by the Bondur and Savin (1995) surface spectral anomaly method, as shown in Figure 1a (top). The anomaly regions vary widely in size and shape, and extend various distances from the wastewater diffuser depending on how far fossil turbulence patches produced by the outfall have been advected and how long they persist. From measured advection speeds of the wastewater and the extent of the anomalies, persistence times (days) of outfall fossil turbulence patches typically exceed $200 N^{-1}$.

The wavelengths of the surface spectral anomalies indicate small-scale soliton-like internal waves exist on the pycnocline. A set of such ISWs measured by thermistor strings in RASP 2004 is shown in Fig. 1b (d). Measured wavelengths match the 43-160 m surface anomaly wavelengths shown in Fig. 1b (c). From the random directions of the spectral anomalies in Figs. 1b (top), 2, 3, 4 (top), and 5 it seems unlikely that ISW waves are caused by the outfall, but their monochromatic wavelength and large energy permits the remote outfall turbulence detection from optical and radar satellites. They may be tidal lee waves, or they may result from fossil-turbulence-waves radiated from powerful bottom turbulence events. The wavelength of FTWs should be the Ozmidov scale at the beginning of fossilization $L_{R_0} = (\epsilon_0 / N^3)^{1/2}$, Fig. 18.

The direction of FTWs radiated by fossilized turbulence events is near-vertical since fossilization occurs at the ambient stratification frequency N . Microstructure studies at the outfall suggest at least 10% of the outfall turbulent kinetic energy is radiated vertically by FTWs. The direction of internal waves radiated from secondary turbulence events (zombie turbulence) is also vertical. Such ZTWs are produced when fossil turbulence patches extract energy from ISWs, Fig. 1c (top). Extraction of quasimonochromatic energy with beaming in a preferred direction (vertical for

internal waves from stratified turbulence) is a maser-action process. The mechanism proposed for the remote detection of RASP outfall turbulence is termed beamed-zombie-turbulence-maser-action. Vertical beaming of turbulent kinetic energy by FTWs from bottom turbulence events is a maser-action process pumped by bottom turbulence that is typically enhanced by zombie turbulence events and ZTWs, and is suggested as the mechanism of remote detection of bottom topography by SAR and by astronauts.

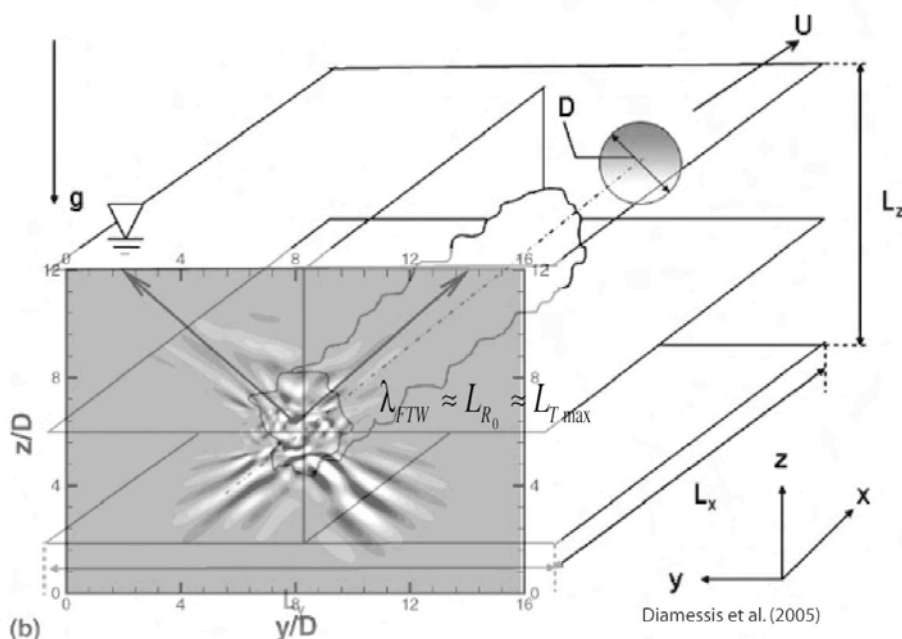


Figure 18: Numerical simulation of a stratified turbulent sphere wake at $Re = 10^4$ by Diamessis et al. (2005). Estimating the maximum Thorpe overturn scale and Ozmidov scale at fossilization from the simulated size of the wake, the fossil turbulence internal waves are shown radiating from the wake at 45° with wavelength $\lambda \approx L_{R_0}$.

The BZTMA mechanism described by KBG is extended in Fig. 1d (bcd) to include tidal lee ISWs detected by SAR radars, Fig. 1a (bottom) and Fig. 1c (bottom). From fossil turbulence theory and deep ocean observations, Gibson (1987), information about submerged ISWs can be moved to the sea surface for detection by fossil-turbulence-waves (FTWs) and secondary zombie-turbulence-waves (ZTWs), Fig. 8 (bottom). Hydrodynamic phase diagrams, Fig. 11, 12, 13 and 14, permit detection and quantification of the process from 10^4 microstructure HPD patches analyzed in the RASP experiments. Thousands of HPD samples were required to detect the dominant outfall actively turbulent patches with $Re/Re_F = \varepsilon/\varepsilon_F \approx \varepsilon_0/\varepsilon_F = Re_0/Re_F \approx 30,000$; that is, in their actively turbulent state, as shown in Fig. 14 by points emphasized by red triangles.

Outfall enhanced ISWs at the 1000 m scales are interpreted as tidal lee waves as shown in Fig. 2 from the Sept. 2, 2002, Ikonos image. Smaller scale ISWs are interpreted as FTWs from bottom turbulence events trapped on the pycnocline. The indicated trapping depth for the waste-field on the Sept. 2, 2002, Ikonos satellite over flight was 42-50 m from vertical MSS profiles in Fig. 7a and Fig. 8 (top). Comparison of HPD plots in Figs. 12, 13, 14 for patches in Figs. 7a, Fig. 8 (top), and Fig. 9 profiles shows that turbulence produced by the wastewater discharge grows in vertical scale as the buoyant plume rises and fossilizes below the trapping depth.

Drogues released at the trapping depth confirm the directions of the surface brightness anomaly maps of Fig. 1b (top), 2, 3, 4 (top), and 5 in SW and SE lobes extending more than 20 km from the diffuser and covering 200 km². The detection effectiveness depends on offshore advection, Fig. 3 b, and Fig. 6. Strong dissipation rates measured near the surface close to the diffuser are larger than ambient surface dissipation rates, Fig. 7b, which supports the conclusion that these $\varepsilon \approx 10^2 \varepsilon_{ambient}$ rates represent surface breaking of near vertically propagating fossil and zombie turbulence waves. The photograph of Fig. 1c (top) confirms this interpretation. See GBKL for further discussion.

Horizontal tows of the MSS at depths above the waste field trapping depth confirm the hypothesis that outfall enhanced mixing should occur above the trapped wastewater depth and in the directions of outfall advection in areas of spectral anomalies, Fig. 3 a), Bondur and Filatov (2003). The enhanced mixing is attributed to outfall fossils extracting energy from soliton-like waves on the 50 m deep pycnocline. Part of the energy is radiated as breaking ZTWs to the surface for detection by the BZTMA mechanism of Fig. 1d (bcd).

Acknowledgements

Fabian Wolk of Rockland Oceanographic Services Inc. and Hartmut Prandke of ISW Wassermesstechnik supplied the MSS equipment, helped plan and carry out the measurements, and made numerous contributions to the validation, analysis and interpretation of the data. Financial support was provided by Directed Technologies, Inc. and 2002-2003 logistical support in Hawaii was provided by Oceanit, Inc.

References

- [1] Alford, M. H., Gregg, M. C., and Merrifield, M. A. 2006. Structure, propagation and mixing of energetic baroclinic tides in Mamala Bay, Oahu, Hawaii, *J. Phys. Oceanogr.*, 36(6), 997-1018.
- [2] Apel, J. R., 2002. Introduction to An Atlas of Internal Solitary Waves, Global Associates, (<http://www.internalwaveatlas.com/>).
- [3] Aguilar, D., Sutherland, B. R., Muraki, D. J. 2005. Deep Sea Res. II, submitted, available at <http://taylor.math.ualberta.ca/~bruce/>.
- [4] Baker, M. A. and Gibson, C. H. 1987. Sampling Turbulence in the Stratified Ocean: Statistical Consequences of Strong Intermittency, *J. of Phys. Oceanogr.*, 17: 10, 1817-1837.

- [5] Baumert, H. Z, Simpson, J. H., and Sundermann, J.; Eds. 2005. *Marine Turbulence, Theories, Observations, and Models*, Cambridge Univ. Press, Cambridge, UK, pp 630.
- [6] Bogucki, D. J., Dickey, T. and Redekopp, L. G. 1997. Sediment resuspension and mixing by resonantly generated internal solitary waves, *J. Phys. Ocean.* 27, 1181-1196.
- [7] Bogucki, D. J., Redekopp, L. G., and Barth, J. 2005. Internal solitary waves in the Coastal Mixing and Optics 1996 experiment: Multimodal structure and resuspension, *J. Geophys. Res.* 110, C02024.
- [8] Bondur, V. G. 2005a. Presentation at RASP 2005 UCSD workshop, Mar. 9-11.
- [9] Bondur, V. G. 2005b. Complex satellite monitoring of coastal water areas, *Proc. of 31st International symposium on remote sensing of environment*, June 20-24, Saint Petersburg, Russian Federation.
- [10] Bondur, V.G., Grebeniuk, Y.V. 2001. Study of the Earth from space, 6, pp. 49-67 (*Issledovania Zemli iz kosmosa*, 6, pp. 49-67, in Russian).
- [11] Bondur, V.G., Filatov, N.N. 2003. Study of physical processes: coastal zone for detecting anthropogenic impact by means of remote sensing. *Proc. of the 7th Workshop on Physical Processes in Natural Waters*, 2 - 5 July, 2003, Russia, Petrozavodsk, 98-103.
- [12] Bondur, V.G., Savin, A.I. 1995. Principle of modeling of signal fields at input into remote sensing equipment of aerospace environment monitoring systems, *Research of the Earth From Space*, 4, 24-33.
- [13] Caldwell, D. R., 1983. Oceanic turbulence: big bangs or continuous creation?, *J. Geophys Res.* 88, C12, 7543-7550.
- [14] Diamessis, P. J., Domaradzki, J. A., Hesthaven, J. S. 2005. A spectral multidomain penalty method model for the simulation of high Reynolds number localized incompressible stratified turbulence, *J. of Comp. Phys.* 202, 298-322.
- [15] Dillon, T. R. 1982. Vertical overturns: A comparison of Thorpe and Ozmidov scales. *J. Geophys. Res.*, 87, 9601-9613.
- [16] Dillon, T. R. 1984. The energetics of overturning structures: Implications for the theory of fossil turbulence, *J. Phys. Oceanogr.*, 14, 541-549.
- [17] Dohan, K. and Sutherland, B. R. 2003, Internal waves generated from a turbulent mixed region, *Physics of Fluids* 15, 488-498.
- [18] Farmer, D. and Armi, L. 1999. The generation and trapping of solitary waves over topography, *Science* 283, 188-190.
- [19] Ferron, B., Mercier, Speer, K., Gargett, A., Polzen, K. 1998. Mixing in the Romanche Fracture Zone, *J. Phys. Oceanogr.*, 28, 1929-1945.
- [20] Finnigan, T. D., Luther, D. S., and Lukas, R. 2002. Observations of Enhanced Diapycnal Mixing near the Hawaiian Ridge, *J. Phys. Oceanogr.*, 32, 2988-3002.
- [21] Flynn, M.R., Sutherland, B.R., 2004. Intrusive gravity currents and internal wave generation in stratified fluid. *Journal of Fluid Mechanics* 514, 355-383.

- [22] Galbraith, P. S. and Kelley, D. E. 1996. Identifying overturns in CTD profiles, *J. At. Oc. Tech.*, 13, 688-702.
- [23] Gibson, C. H. 1980. Fossil temperature, salinity, and vorticity turbulence in the ocean, in *Marine Turbulence*, J. Nihoul (Ed.), Elsevier Publishing Co., Amsterdam, 221-257.
- [24] Gibson, C. H. 1983. Turbulence in the Equatorial Undercurrent Core, in *Hydrodynamics of the Equatorial Ocean (Proceedings of the 14th International Liege Colloquium on Ocean Hydrodynamics, (Liege, May 1982), Vol. 36, J. C. H. Nihoul (Ed.), Elsevier Oceanography Series, Elsevier Publishing Company, Amsterdam 131-154.*
- [25] Gibson, C. H. 1986. Internal waves, fossil turbulence, and composite ocean microstructure spectra, *J. Fluid Mech.* 168, 89-117.
- [26] Gibson, C. H. 1987. Oceanic turbulence: big bangs and continuous creation, *PhysicoChemical Hydrodynamics*, 8(1), 1-22.
- [27] Gibson, C. H. 1991a. Kolmogorov similarity hypotheses for scalar fields: sampling intermittent turbulent mixing in the ocean and galaxy, in *Turbulence and stochastic processes: Kolmogorov's ideas 50 years on*, Proceedings of the Royal Society London, Ser. A, 434, 1890, 149-164; <http://xxx.lanl.gov, astro-ph/9904269>.
- [28] Gibson, C. H. 1991b. Laboratory, numerical, and oceanic fossil turbulence in rotating and stratified flows. *J. Geophys. Res.*, 96(C7), 12,549–12,566.
- [29] Gibson, C. H. 1991c. Turbulence, mixing, and heat flux in the ocean main thermocline, *J. Geophys. Res.*, 96: C7, 20,403-20,420.
- [30] Gibson, C. H., V. Nabatov, R. Ozmidov 1993. Measurements of turbulence and fossil turbulence near Ampere Seamount, *Dynamics of Atmospheres and Oceans*, 19, 175-204.
- [31] Gibson, C. H. 1999. Fossil turbulence revisited, *J. of Marine Systems*, 21(1-4), 147-167; <http://xxx.lanl.gov, astro-ph/9904237>.
- [32] Gibson, C. H. 2004. The first turbulence and first fossil turbulence. *Flow, Turbulence and Combustion*, 72, 161-179.
- [33] Gibson, C. H., Bondur, V. G., and Keeler, R. N. 2006. Energetics of the beamed zombie turbulence maser action mechanism for remote detection of submerged oceanic turbulence, *J. Appl. Fluid Mech.* (in press), <http://www-acs.ucsd.edu/~ir118>, GBKL.
- [34] Grebeniuk, Y. V. 2005. Presentation at RASP 2005 UCSD workshop, Mar. 9-11.
- [35] Gregg, M. C., Sanford, T. B. & Winkel, D. P. 2003. Reduced mixing from the breaking of internal waves in equatorial waters, *Nature* 422, 513–515.
- [36] Gregg, M. C. 1977. a. A comparison of finestructure spectra from the main thermocline, *J. Phys. Oceanogr.* 7, 33-40; also, b. Variations in the intensity of small-scale mixing in the main thermocline, *J. Phys. Oceanogr.* 7, 436-454.
- [37] Gregg, M. C. 1987. Diapycnal mixing in the thermocline, *J. Geophys. Res.* 92, 5249-5286.
- [38] Keeler, R. N., Bondur, V. G., and Gibson, C. H. 2005. Optical satellite imagery detection of internal wave effects from a submerged turbulent outfall

- in the stratified ocean, *Geophys. Res. Lett.*, 32, L12610, doi:10.1029/2005GL022390, KBG.
- [39] Leung, P. T. and Gibson, C. H. 2004. Turbulence and fossil turbulence in oceans and lakes, *Chinese Journal of Oceanology and Limnology*, 22(1), 1-23. <http://xxx.lanl.gov/astro-ph/0310101>.
- [40] Linden, P. F. 1975. The deepening of a mixed layer in a stratified fluid, *J. Fluid Mech.* 71, 385-405.
- [41] LaFond, E. C., 1962. Ch. 22. Internal waves, in *The Sea*, vol. 1 *Physical Oceanography*, p731-763.
- [42] Maxworthy, T., 1979. A note on the internal solitary waves produced by tidal flow over a three dimensional ridge. *J. Geophys. Res.* 84, 338-346.
- [43] Munk, W. H., 1966: Abyssal recipes. *Deep-Sea Res.*, 13, 207-230.
- [44] Munk, W. H., and C. Wunsch, 1998: Abyssal recipes II: Energetics of tidal and wind mixing. *Deep-Sea Res.*, 45, 1978-2010.
- [45] Moum, J. N., Farmer, D. M., Smyth, W. D., Armi, L., Vagle, S. 2003. Structure and generation of turbulence at interfaces strained by internal solitary waves propagating shoreward over the continental shelf, *J. of Physical Oceanography*, vol.33, no.10, Oct. 2003, pp.2093-112.
- [46] Moum, J. N., and Smyth, W. D. 2005. The pressure disturbance of a nonlinear internal wave train, *J. Fluid Mech.*, submitted.
- [47] Nasmyth 1980. Towed vehicles and submersibles, *Air-sea interaction, Instruments and Methods*, P. Dobson, L. Hasse, and R. Davis Eds., Plenum Press, NY, 739-765.
- [48] Pinkel, R., M. Merrifield, M. McPhaden, J. Picaut, S. Rutledge, D. Siegel, and L. Washburn, 1997. Solitary waves in the western Equatorial Pacific Ocean. *Geophys. Res. Lett.*, 24 (13), 1603.
- [49] Polzin, K. L., Toole, J. M., Ledwell, J. R., Schmitt, R. W. 1997. Spatial variability of turbulent mixing in the abyssal ocean, *Science* 276, 93.
- [50] Prandke, H., T. Neumann and A. Stips, 1988. MSS 86-ein neues Messsystem zur Untersuchung der Mikrostruktur der bodennahen Wasserschicht im Meer.- *Beiträge zur Meereskunde*, 58, 71-72.
- [51] Prandke, H. and A. Stips 1998. Microstructure profiler to study mixing and turbulent transport processes.- *OCEANS'98 Conference proceedings Vol.1 IEEE* 179-183.
- [52] Prandke, H. and A. Stips 1992. A model of Baltic thermocline turbulence patches, deduced from experimental investigations, *Cont. Shelf Res.*, 12, 643-659.
- [53] Rudnick, D. L., T. J. Boyd, R. E. Brainard, G. S. Carter, G. D. Egbert, M. C. Gregg, P. E. Holloway, J. M. Klymak, E. Kunze, C. M. Lee, M. D. Levine, D. S. Luther, J. P. Martin, M. A. Merrifield, J. N. Moum, J. D. Nash, R. Pinkel, L. Rainville, T. B. Sanford, 2003: From tides to mixing along the Hawaiian Ridge, *Science*, 301(8), 355-357.
- [54] Sutherland, B. R. 2005. Presentation at RASP 2005 UCSD workshop, Mar. 9-11.

- [55] Sutherland, B. R. 2001. Finite-amplitude internal wavepacket dispersion and breaking, *J. Fluid Mech.* 429, 343-380.
- [56] Sutherland, B. R. and Linden, P. F. 1998. Internal wave excitation from stratified flow over a thin barrier, *J. Fluid Mech.* 377, 223-252.
- [57] Sutherland, B. R., Dalziel, S. B., Hughes, G. O., and Linden, P. F. 1999. Visualisation and measurement of internal waves by 'synthetic schlieren.' Part 1: Vertically oscillating cylinder, *J. Fluid Mech.* 390, 93.
- [58] Sutherland, B. R., Flynn, M. R. and Dohan, K. 2004. Internal wave excitation from a collapsing mixed region, *Deep-Sea Research II* 51, 2889-2904.
- [59] Sutherland, B. R. and Yewchuk, K. 2004. Internal wave tunneling, *J. Fluid Mech.* 511, 125-134.
- [60] Thorpe, S. A. 1977: Turbulence and mixing in a Scottish loch. *Philos. Trans. Roy. Soc. London.* A286, 125-181.
- [61] Williams, R. B and Gibson, C. H. 1974. Direct measurements of turbulence in the Pacific Equatorial Undercurrent, *J. Phys. Ocean.*, 4, 1, 104-108.
- [62] Wolk, F., Yamazaki, H., Seuront, L. and Lueck, R. G., 2002. A new free-fall profiler for measuring biophysical microstructure, *J. Atm. and Ocean. Tech.*, 19, 780-793.
- [63] Wolk, F., H. Prandke, H. and C. H. Gibson 2004. Turbulence measurements support satellite observations, *Sea Technology*, August, 45, 47-53.